aerospace

MDPI

Article

Coupling of Advanced Guidance and Robust Control for the Descent and Precise Landing of Reusable Launchers

Alice De Oliveira * and Michèle Lavagna

Department of Aerospace Science & Technology, Politecnico di Milano, Via La Masa 34, 20156 Milan, Italy
* Correspondence: alice.deoliveira@polimi.it

Abstract: This paper investigates the coupling of successive convex optimization guidance with robust structured H_∞ control for the descent and precise landing of Reusable Launch Vehicles (RLVs). More particularly, this Guidance and Control (G&C) system is foreseen to be integrated into a nonlinear six-degree-of-freedom RLV controlled dynamics simulator which covers the aerodynamic and powered descent phase until vertical landing of a first-stage rocket equipped with a thrust vector control system and steerable planar fins. A cost function strategy analysis is performed to find out the most efficient one to be implemented in closed-loop with the robust control system and the vehicle flight mechanics involved. In addition, the controller synthesis via structured H_∞ is thoroughly described. The latter are built at different points of the descent trajectory using Proportional-Integral-Derivative (PID)-like structures with feedback on the attitude angles, rates, and lateral body velocities. The architecture is verified through linear analyses as well as nonlinear cases with the aforementioned simulator, and the G&C approach is validated by comparing the performance and robustness with a baseline system in nominal conditions as well as in the presence of perturbations. The overall results show that the proposed G&C system represents a relevant candidate for realistic descent flight and precise landing phase for reusable launchers.

Keywords: RLV; G&C; aerodynamic and powered descent; precise landing; descent and landing dynamics; successive convex optimization; structured H_∞ synthesis; TVC; aerodynamic steering

Citation: De Oliveira, A.; Lavagna, M. Coupling of Advanced Guidance and Robust Control for the Descent and Precise Landing of Reusable Launchers. *Aerospace* **2024**, *11*, 914. https://doi.org/10.3390/aerospace11110914

Academic Editor: Pedro Simplicio

Received: 27 September 2024
Revised: 29 October 2024
Accepted: 31 October 2024
Published: 7 November 2024

1. Introduction

Developing reusable launchers has become one of the key aspects of the space race for any country seeking independent and sustainable access to space. In December 2015, the US private company SpaceX showed the technical feasibility of launcher reusability by landing its *Falcon 9* first stage after having delivered a payload into orbit [1]. Two years later, the same company demonstrated the cost effectiveness of such a technology by reusing a recovered first stage for another mission [2]. SpaceX is today one of the major space companies and is currently developing its *Super Heavy* rocket equipped with the *Starship* spacecraft with the objective of carrying both crew and cargo on long-duration interplanetary flights and to allow humanity to return to the Moon and travel to Mars and beyond. In June 2024, *Starship* 29 (S29) and its *Super Heavy* Booster (B11) marked the first integrated test flight, where both stages successfully re-entered and performed a powered vertical landing over the ocean surface. Meanwhile, Rocket Lab's *Electron* microlauncher is well integrated in the market, and the company is currently developing its medium-lift rocket *Neutron* [3]. Blue Origin is also focusing on advanced reusable launchers such as *New Shepard*, a suborbital launch vehicle designed for space tourism, and *New Glenn*, a heavy-lift reusable rocket that should be able to carry heavy payloads to Earth orbit and beyond [4]. Outside of the United States and in what can be described as the new space race, China [5] and India [6] are actively working on their own reusable launchers. In Europe, various programmes are underway, such as *Themis* from the European Space Agency (ESA), National Center for Space Studies (CNES), and ArianeGroup, which is a

first-stage rocket demonstrator aimed at paving the way for the future European reusable launcher, *Ariane Next* [7]. Additionally, the collaborative project CALLISTO, involving the German Aerospace Center (DLR), Japan Aerospace Exploration Agency (JAXA), and CNES, is focused on the development of a European/Japanese reusable rocket demonstrator [8].

Following similar guidelines, the European project Advancing Space Access Capabilities—Reusability and Multiple Satellite Injection (ASCenSIon) has been initiated as an innovative training network involving multiple public institutions and companies across Europe in order to study the critical technologies for the development of a Reusable Launch Vehicle (RLV) capable of injecting multiple payloads into multiple orbits. More particularly, one of the research fields involved in this project aims to study the design of the Guidance and Control (G&C) system for the vehicle descent and precise landing on Earth, essential for reusability. In fact, this flight phase is very challenging as it depends on multiple parameters, which are further complicated by the dense terrestrial atmosphere [9]. During descent, the vehicle is subjected to fast, dynamics changes, partly induced by external loads such as lift, drag, and wind but also by the actuation commands to fulfil the landing constraints satisfaction and vehicle integrity preservation. Recovering a first-stage launcher was made possible in the last decade by the development of advanced and robust computational methods able to generate in real time the reference trajectory to be followed according to the actual flight conditions, and then to command the optimal vehicle's actuator deflections to steer the vehicle to the landing site. Despite the success of the aforementioned commercial space companies, some standing problems, such as the aerodynamic and powered descent of the launcher, require further understanding.

One of the critical aspects of G&C design for the descent and precise landing of reusable rockets is the development of a robust control strategy capable of counteracting disturbances and uncertainties while satisfying the strict accuracy requirements associated with pinpoint landing. This synthesis is further complicated by the need for a real-time guidance algorithm to update onboard the optimal trajectory to be followed by the vehicle, which therefore requires that the controller be capable of tracking multiple types of possible references. In fact, thanks to the increase in computational power available onboard, recent progress has shown that convex optimization is among the key technologies to enable autonomous and onboard real-time trajectory planning, and therefore pinpoint landing. More particularly, advanced methods such as successive convex optimization [10] and pseudospectral convex optimization [11] enable the definition of a fuel-optimal trajectory problem in which nonlinearities (e.g., aerodynamics) or non-convex constraints can be integrated [8,12,13] and that can be solved in polynomial times with efficient solvers. When implemented in a closed-loop fashion, this advanced guidance design enables the correction of potential trajectory tracking discrepancies caused by uncertainties within the algorithm's embedded models or external disturbances.

As demonstrated by the current state-of-the-art in launcher control design [14,15], classical linear control theory represents a rich heritage with many applications. This choice was motivated by its relative ease of implementation and the possibility of using gain-scheduling techniques to adapt to nonlinear systems. Nevertheless, these methods are well-adapted to the control system design of Single-Input Single-Output (SISO) systems, such as, for example, a reusable rocket using a Thrust Vector Control (TVC) system as the unique actuator. The implementation of Multiple-Input Multiple-Output (MIMO) control systems then becomes complex since every channel is addressed in a single-loop fashion. However, this capability is required for the future generation of reusable rockets, which also commonly use fin-based aerodynamic steering in addition to the TVC system to enhance control authority. Furthermore, model uncertainties are not accurately considered in the design process, developed only with nominal conditions and stability margin requirements. All these issues result in an extensive (in terms of both time and cost) verification and validation campaign with many iterations and Monte-Carlo analyses to assess the performance and robustness of the control system.

To overcome these drawbacks, the H_∞ family of methods, introduced a few years ago [16], provides a powerful solution for robust control design. It relies on defining the control requirements in the frequency domain in terms of weighting functions and minimizing the maximum gain of the resulting weighted system from the exogenous inputs to the outputs to be controlled. The control–plant interaction is modelled through a Linear Fractional Transformation (LFT) that represents the feedback action. Furthermore, the structured H_∞ method [17] allows one to directly impose a specific control structure—like a Proportional-Integral-Derivative (PID), enabling the reuse of gain-scheduling techniques—and to consider parametric uncertainties for enhanced robustness. This technology was studied in the United States for the *Ares-I* programme, later for the *Space Launch System* programme [18], and in Europe for *Ariane 5* [19] and the future generation of European launchers [20]. In recent years, several studies have emerged regarding this method for the descent and landing phases of vehicles and have shown promising results. Although structured H_∞ was first studied mainly for the ascent phase of the *VEGA* launcher recovering the baseline control structure [21], some analyses were further performed in the descent phase [22]. Furthermore, interesting cases for the aerodynamic descent of reusable rockets have been exploited within the framework of CALLISTO where, first, decoupled attitude and translational channels were considered for the design of robust controllers on each control axis [23], before a unified control was considered for both position and attitude with a robustness analysis to account for uncertainties [24]. Finally, a multi-plant control design approach with fully-coupled translational and attitude dynamics was studied as a solution to better consider the range of trajectories coming from the online guidance algorithm during flight [25].

It is clear from the available literature that, while this technology has been largely explored for the ascent phase of conventional (i.e., non-reusable) launch vehicles, there is still room for exploiting its capabilities during the descent and precise landing phase of reusable rockets. Furthermore, among most of the aforementioned literature, only the aerodynamic descent phase using steerable planar fins was considered, and the powered-descent phase combining fins and TVC was treated only in Ref. [22]. This paper investigates the problem of coupling advanced guidance and robust control systems for the descent and precise landing of RLVs, involving fin-based aerodynamic steering and the TVC system simultaneously in the control action. It exploits the room for improvement that comes from the reusable launcher controlled dynamics simulator, developed in previous work under the ASCenSIon project [26]. This simulator precisely models the existing interactions between the environment with its potential disturbances and uncertainties, the corresponding nonlinear Six-Degree-of-Freedom (6-DoF) equations of motion, the actuators, and the G&C system. In that paper, the latter was proposed as the baseline for preliminary assessments, which involved a successive convex optimization algorithm maximizing the vehicle final mass and a control system for which the MIMO formulation induced by the coupling of TVC and steerable planar fins is simplified to a series of SISO systems to apply classical linear control theory. In this paper, from the G&C system of Ref. [26], first the guidance algorithm is improved by using a cost function strategy that involves both minimization of time of flight and maximization of final mass. The latter still copes with mission requirements and can also be efficiently coupled with the other building blocks. Second, a new architecture is introduced for control synthesis through structured H_∞. The latter is simultaneously tuning gain-scheduled PID controllers for both planar fins and the TVC system through feedback on attitude and velocity (with the main focus on attitude). The robustness of the control system obtained is assessed through linear analysis and nonlinear simulations with the aforementioned tool, under nominal and dispersed conditions. Therefore, the main contribution of this work is twofold: the design of a robust control strategy through H_∞ synthesis combining two actuators, TVC, and steerable planar fins, followed by the performance assessment of the integrated G&C design through a 6-DoF nonlinear simulator. To the best of the authors' knowledge, this is the first time that such a control strategy is coupled with an advanced guidance algorithm for the entire descent and landing problem

of a reusable rocket and assessed in a realistic scenario. Furthermore, this paper takes the perspective of integrated analysis rather than a compartmentalized design of guidance and control strategies. In fact, such strategies are emerging in the literature: Ref. [27] combines an optimal guidance strategy with a linear quadratic regulator control approach for the rocket-powered descent phase, while Ref. [28] proposes an integrated and adaptive G&C design via reinforcement meta-learning for air-to-air missiles.

The paper is organised as follows. Section 2 introduces the modelling of the nonlinear controlled dynamics involved in reusable launcher descent and precise landing. More particularly, Section 3 describes the guidance method embedded in a closed-loop fashion in the simulator. Then, Section 4 formulates the robust control design via structured H_∞, with weighting functions adequately chosen according to the available requirements. The synthesized controllers are assessed through classical linear analysis, and robustness stability and performance are assessed via structured singular value μ-analysis. Subsequently, in Section 5, the synthesized controllers are embedded in the controlled dynamics simulator, therefore coupled with the guidance system, and assessed through nonlinear analysis under both nominal and dispersed conditions. Finally, conclusions regarding the work performed are provided in Section 6.

2. Reusable Launcher Controlled Dynamics Simulator

This section describes the nonlinear 6-DoF descent dynamics of a Vertical Take-off Vertical Landing (VTVL) vehicle first-stage booster modelled through rigid-body motion with varying mass, subjected to external forces induced by the terrestrial atmosphere and controlled through embedded closed-loop guidance and control strategies. This paper relies on the controlled dynamics simulator developed by the authors and adapted from Ref. [29] to study the efficiency of aerodynamic steering and conventional G&C techniques [26]. The latter is illustrated in Figure 1, showcasing the interactions between all building blocks, from the G&C systems to the actuators, vehicle dynamics, and environment.

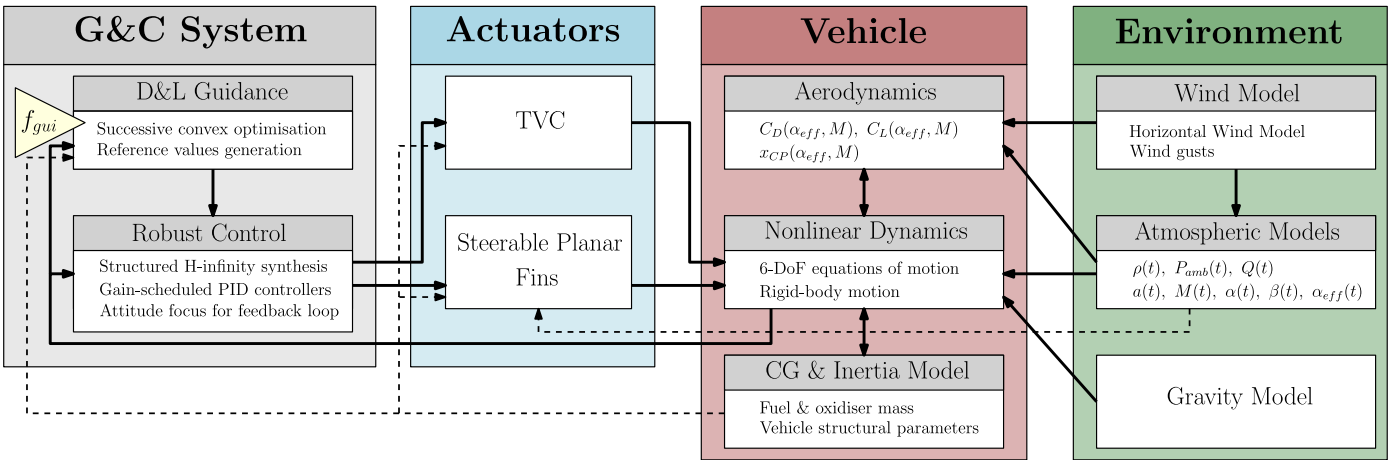

Figure 1. 6-DoF RLV controlled dynamics simulator description.

The latter includes standard G&C algorithms, where a thrust vector is commanded by the guidance subsystem and then converted to the reference pitch angle, $\theta_{ref}(t)$, and yaw, $\psi_{ref}(t)$, rates $\dot{\theta}_{ref}(t)$ and $\dot{\psi}_{ref}(t)$, lateral body velocities $\dot{y}_{B,ref}(t)$ and $\dot{z}_{B,ref}(t)$, and thrust magnitude T_{ref}. The control subsystem then generates the necessary commands to correct the deviations between the reference and actual attitude angles in terms of TVC gimbal deflections, $\{\beta_{TVC,y}, \beta_{TVC,z}\}$, and fin deflections, $\{\beta_{fin,y}, \beta_{fin,z}\}$. The guidance subsystem is based on a successive convex optimization algorithm. The reference trajectory generated is updated with a user-specified frequency, f_{gui}, at which the guidance subsystem is re-executed. Concerning the control subsystem, it relies on the use of feedback control through gain-scheduled PID controllers synthesized via structured H_∞ synthesis, decoupling pitch

and yaw axes based on the assumption of low roll rate. These two subsystems will be better defined in Section 3 and Section 4, respectively.

The equations of motion are written in the landing site-centred inertial and the vehicle's body-fixed reference frames using the following initial state vector, $\mathbf{x}_I(0) = \begin{bmatrix} m(0) & \mathbf{r}_I^T(0) & \mathbf{v}_I^T(0) & \mathbf{q}_B^I(0)^T & \boldsymbol{\omega}_B^T(0) \end{bmatrix}$, and, for the sake of simplicity, based on the assumptions that the vehicle is a rigid body with no effect induced by the varying mass (e.g., propellant sloshing) and structural flexibilities. The mass depletion dynamics are modelled by an affine function of the thrust magnitude as follows:

$$\dot{m}(t) = -\frac{||\mathbf{F}_{TVC,I}(t)||_2}{I_{sp} g_0} - \frac{A_{nozzle} P_{amb}(t)}{I_{sp} g_0} \tag{1}$$

where I_{sp} is the vacuum specific impulse of the engine, assumed to be constant for simplicity, and A_{nozzle} is the nozzle exit area of the engine. $\mathbf{F}_{TVC,I}(t) \in \mathbb{R}^3$ is the thrust vector coming from the TVC system, represented in the inertial reference frame. The second term is related to the reduction of the specific impulse due to the atmospheric back-pressure [10].

The translational states, position, and velocity of the vehicle in the inertial reference frame, $\mathbf{r}_I(t) \in \mathbb{R}^3$ and $\mathbf{v}_I(t) \in \mathbb{R}^3$, are governed by the following dynamics:

$$\begin{aligned} \dot{\mathbf{r}}_I(t) &= \mathbf{v}_I(t) \\ \dot{\mathbf{v}}_I(t) &= \frac{1}{m(t)} \Big[\mathbf{F}_{TVC,I}(t) + \mathbf{F}_{aero,I}(t) + \mathbf{F}_{fins,I}(t) \Big] + \mathbf{g}_I(t) \end{aligned} \tag{2}$$

where $\mathbf{F}_{aero,I}(t) \in \mathbb{R}^3$ described the aerodynamic force acting on the vehicle in the inertial reference frame, $\mathbf{F}_{fins,I}(t) \in \mathbb{R}^3$ represents the control force generated by the planar fins, and $\mathbf{g}_I(t)$ is the gravitational field defined in the inertial frame.

Then, the attitude states are governed by the following rotational dynamics, using the following quaternion-based kinematics equation:

$$\begin{aligned} \dot{\mathbf{q}}_B^I(t) &= \frac{1}{2} \begin{bmatrix} q_4(t) & -q_3(t) & q_2(t) \\ q_3(t) & q_4(t) & -q_1(t) \\ -q_2(t) & q_1(t) & q_4(t) \\ -q_1(t) & -q_2(t) & -q_3(t) \end{bmatrix} \boldsymbol{\omega}_B(t) \\ \dot{\boldsymbol{\omega}}_B(t) &= J^{-1}(t) \Big[\mathbf{M}_{TVC,B}(t) + \mathbf{M}_{aero,B}(t) + \mathbf{M}_{fins,B}(t) - \boldsymbol{\omega}_B(t) \times J(t) \boldsymbol{\omega}_B \Big] \end{aligned} \tag{3}$$

where $J(t) = \text{diag}\big(\begin{bmatrix} J_A(t) & J_N(t) & J_N(t) \end{bmatrix}\big)$ is the inertia matrix of the vehicle and $\mathbf{M}_{aero,B}(t) \in \mathbb{R}^3$, $\mathbf{M}_{TVC,B}(t) \in \mathbb{R}^3$, and $\mathbf{M}_{fins,B}(t) \in \mathbb{R}^3$ represent the aerodynamic and control torques acting on the vehicle. In Equation (3), the coupling between angular velocity and inertia along the three axes, and the effect of centroid movement on the inertia caused by mass consumption, are ignored.

For the computation of the aerodynamic forces and moments generated by the vehicle, it is necessary to define an additional reference frame, the so-called velocity reference frame. The latter is fixed to the vehicle's Center of Gravity (CG), with its x-axis directed along the wind-relative vector, $\mathbf{v}_{air}(t)$, so that the transformation from the body-fixed to the velocity reference frame can be represented by two aerodynamic angles: the angle of attack, $\alpha(t)$, and the sideslip angle, $\beta(t)$ [30]. Then, the aerodynamic characteristics depend on the vehicle's external shape with its reference area and on the instantaneous dynamic pressure, which is defined as follows:

$$Q(t) = \frac{1}{2} \rho(t) ||\mathbf{v}_{air}(t)||^2 \tag{4}$$

where $\mathbf{v}_{air}(t)$ accounts for the vehicle's inertial velocity and wind gusts, and the atmospheric density $\rho(t)$ is generated using the Committee on Extension to the Standard Atmosphere model [31] (like the ambient pressure, $P_{amb}(t)$, and the speed of sound, $a(t)$). The aerodynamic drag and lift coefficients, as well as the Center of Pressure (CP) position,

are estimated from available look-up tables as a function of the effective angle of attack, $\alpha_{eff}(t) = \sqrt{\alpha^2(t) + \beta^2(t)}$, and the Mach number, $M(t)$ [32].

3. Guidance Approach

This section describes the Descent and Landing (D&L) guidance strategy adopted in the previously defined controlled dynamics simulator, which is responsible for the real-time generation of a fuel-optimal reference trajectory with thrust, attitude, and velocity commands to be sent to the robust control subsystem. As mentioned in Section 1, the literature of guidance methods for the reusable launcher descent and landing phase is now focusing on advanced computational techniques, among them successive convex optimization or pseudospectral convex optimization, therefore giving up to the traditional guidance schemes commonly implemented for the ascent phase and for which path constraints could not be enforced. In this paper, the direct method, successive convex optimization, is employed and analysed before being implemented in the controlled dynamics simulator for closed-loop integration assessment.

Convex optimization guidance consists of transforming the fuel-optimal trajectory problem into a convex one, more particularly into a Second-Order Cone Programming (SOCP) problem, which can be solved with efficient solvers in polynomial time. The recent increase in the computational power available onboard made the real-time implementation of these algorithms possible. The challenging task relies on converting the non-convex state and control constraints into convex forms [33]. Then, successive convex optimization can be applied to approximate the remaining nonlinearities in the optimal landing problem, such as the aerodynamic effects previously ignored. It consists of iteratively solving SOCP convex optimization subproblems in which the non-convex dynamics and constraints are repeatedly linearised using information coming from the previous iteration solution. This algorithm was first developed in Ref. [34] and then adapted in different ways [12,13]. In this study, the strategy defined in Ref. [10] is leveraged to be applicable in a closed-loop fashion. The algorithm is thoroughly detailed in Ref. [26] from the same authors and summarized hereafter. First, the guidance strategy is detailed in Section 3.1, and the corresponding SOCP problem is described in Section 3.2.

3.1. Successive Convex Optimization Strategy

The successive convex optimization guidance algorithm was implemented in MATLAB (R2021b) using the CVX library [35] to formulate the convex problem and the ECOS routine [36] to solve them. In each simulation instance defined by the simulation rate, $f_{sim} = 10^3$ Hz, the reference thrust profile, $\mathbf{T}_{B,ref}(t)$, the reference attitude angles, $\{\theta_{ref}(t), \psi_{ref}(t)\}$, rates, $\{\dot{\theta}_{ref}(t), \dot{\psi}_{ref}(t)\}$, and the reference body velocities, $\{\dot{y}_{B,ref}(t), \dot{z}_{B,ref}(t)\}$, are calculated from the most recent guidance solution by linear interpolation. In fact, as mentioned above, this solution is stored as an online lookup table, which is updated at each guidance step, with the guidance update frequency $f_{gui} = 0.1$ Hz, that is, every 10 s. Note that, to avoid adding complexity, the steerable planar fins are not considered as control inputs in the guidance problem. The guidance algorithm inside the "D&L Guidance" building block of the simulator is schematized in Figure 2.

First, the state and control vectors, as well as the final time, t_f, which is also an optimization variable in this problem, are initialized. A linear interpolation of the discrete state variables under the initial and final conditions is used for the initial state vector, while the initial control vector is taken as matching the gravitational force [26]. Once the initial guess is defined, we enter the successive convex optimization loop, which consists of solving the SOCP problem several times until reaching the user-defined maximum iterations number, i_{max}, or the tolerance relative to the trust regions radius, Δ_{tol}. Then, to enable the formulation of the SOCP subproblems, the optimal control problem must be converted into a finite-dimensional parameter optimization problem. Therefore, the trajectory and optimization variables are discretized into K uniformly spaced points, ranging from the

current instant of time, t_c, to the final time, t_f. At each guidance step, the time vector is divided in that way:

$$t[k] = \frac{k-1}{K-1} t_f, \quad k \in [1, K] \tag{5}$$

and because the estimated time of flight $t_f \to 0$ as $t \to ToF$, where ToF is the actual time of flight achieved by the simulation, the accuracy of the discretization becomes more precise towards the end. More particularly, the sampling time is given by $T_s = t_f/(K-1)$. The linearization and discretization methods are explained in the next subsection, together with the definition of the SOCP problem.

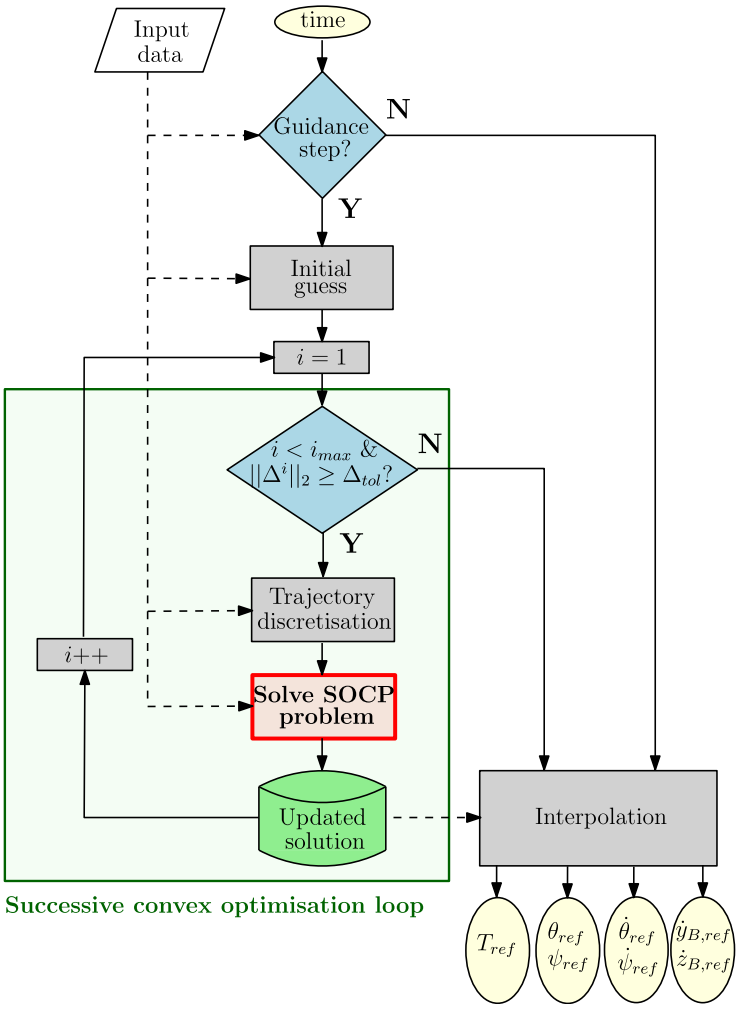

Figure 2. "D&L Guidance" block description, adapted from Ref. [13].

When the optimization algorithm converges to an optimal solution, this reference trajectory is saved to be used for the next iteration, or, if the exit criterion of the successive convex optimization routine is met, is transferred to the online look-up table from where the actual reference parameters corresponding to the simulation instance can be generated. In this study, this involves the reference thrust magnitude profile, $T_{ref}(t)$, the reference pitch and yaw angle profiles, respectively $\theta_{ref}(t)$ and $\psi_{ref}(t)$, rates, respectively $\dot{\theta}_{ref}(t)$ and $\dot{\psi}_{ref}(t)$, and the reference body velocities, $\dot{y}_{B,ref}(t)$ and $\dot{z}_{B,ref}(t)$.

3.2. SOCP Problem

The SOCP optimization problem obtained in Ref. [26], which is solved iteratively in the successive convex optimization algorithm, is summarized in Figure 3.

$$\min_{\sigma^i, \mathbf{u}^i[k]} \quad J = \sigma^i - m^i[K] + w_{\boldsymbol{\nu}} S^i_{\boldsymbol{\nu}} + w_{\boldsymbol{\Delta}_{\mathbf{x},\mathbf{u}}} S^i_{\boldsymbol{\Delta}_{\mathbf{x},\mathbf{u}}} + w_{\Delta_\sigma} \Delta^i_\sigma,$$

s.t.:

Boundary conditions

$$m^i[1] = m_c,\ \mathbf{r}^i_I[1] = \mathbf{r}_{I,c},\ \mathbf{v}^i_I[1] = \mathbf{v}_{I,c},\ \boldsymbol{\omega}^i_B[1] = \boldsymbol{\omega}_{B,c},$$
$$\mathbf{q}^{i,I}_B[1] = \mathbf{q}^I_{B,c}, \quad \text{if not the first run}$$
$$\mathbf{r}^i_I[K] = \mathbf{r}_{I,d},\ \mathbf{v}^i_I[K] = \mathbf{v}_{I,d},\ \mathbf{q}^{i,I}_B[K] = \mathbf{q}^I_{B,d},\ \boldsymbol{\omega}^i_B[K] = \boldsymbol{\omega}_{B,d}$$

Dynamics equations, $\forall k \in [1, K-1]$

$$\mathbf{x}^i[k+1] = \bar{\mathbf{A}}[k]\mathbf{x}^i[k] + \bar{\mathbf{B}}[k]\mathbf{u}^i[k] + \sigma\bar{\boldsymbol{\Sigma}}[k] + \bar{\mathbf{z}}^i[k] + \boldsymbol{\nu}^i[k]$$

State constraints, $\forall k \in [1, K]$

$$m^i[k] \geq m_{dry},\ \mathbf{e}_1 \cdot \mathbf{r}^i_I[k] \geq \tan(\gamma_{gs}) \left|\left| \begin{bmatrix} \mathbf{e}_2 & \mathbf{e}_3 \end{bmatrix}^T \mathbf{r}^i_I[k] \right|\right|_2$$
$$\cos(\theta_{max}) \leq \mathbf{e}^T_{I,1}\, \mathbf{R}^{i,B}_I[k]\, \mathbf{e}_{B,1},\ ||\boldsymbol{\omega}^i_B[k]||_2 \leq \omega_{max}$$
$$||\mathbf{q}^{I,i-1}_B[k]||_2 + \frac{\mathbf{q}^{I,i-1}_B[k]^T}{||\mathbf{q}^{I,i-1}_B[k]||_2}(\mathbf{q}^{I,i}_B[k] - \mathbf{q}^{I,i-1}_B[k]) = 1$$

Control constraints, $\forall k \in [1, K-1]$

$$\cos(\delta_{max})||\mathbf{T}^i_{B,ref}[k]||_2 \leq \mathbf{e}_1 \cdot \mathbf{T}^i_{B,ref}[k]$$
$$h_T(\mathbf{u}^{i-1}[k]) + \left.\frac{\partial h_T}{\partial \mathbf{u}}\right|_{\mathbf{u}^{i-1}[k]} (\mathbf{u}^i[k] - \mathbf{u}^{i-1}[k]) \leq 0$$
$$||\mathbf{T}^i_{B,ref}[k]||_2 \leq T_{max}$$

Trust regions, $\forall k \in [1, K-1]$

$$||\mathbf{x}^i[k] - \mathbf{x}^{i-1}[k]||_2 + ||\mathbf{u}^i[k] - \mathbf{u}^{i-1}[k]||_2 \leq \Delta^i_{\mathbf{x},\mathbf{u}}[k]$$
$$||\boldsymbol{\Delta}^i_{\mathbf{x},\mathbf{u}}||_2 \leq S^i_{\boldsymbol{\Delta}_{\mathbf{x},\mathbf{u}}}$$
$$||\sigma^i - \sigma^{i-1}||_2 \leq \Delta^i_\sigma$$

Virtual controls, $\forall k \in [1, K-1]$

$$||\bar{\boldsymbol{\nu}}^i||_2 \leq S^i_{\boldsymbol{\nu}}$$

Figure 3. SOCP problem.

The 6-DoF descent dynamics of a powered-only, first-stage booster are linearized and discretized about the solution of the previous iteration through a first-order Taylor expansion approximation and using a zero-order-hold interpolation scheme. Note that only the thrust force is considered as the control input, so that the contribution of the fins is ignored through the guidance logic. Before this process, the time of flight is normalized from $t \in [t_c, t_f]$ to $\tau \in [0, 1]$, where τ is the normalized time of flight, to obtain a fixed-final-time optimization problem. Summarizing the nonlinear dynamics as $\dot{\mathbf{x}}(t) = f(\mathbf{x}(t), \mathbf{u}(t))$, with $\mathbf{x}(t) = \begin{bmatrix} m(t) & \mathbf{r}^T_I(t) & \mathbf{v}^T_I(t) & \mathbf{q}^I_B(t)^T & \boldsymbol{\omega}^T_B(t) \end{bmatrix}^T$ as the state vector and $\mathbf{u}(t) = \mathbf{T}_{B,ref}(t)$ as the control vector, they can be rewritten as follows:

$$\dot{\mathbf{x}}(t) = \frac{\mathrm{d}\tau}{\mathrm{d}t}\frac{\mathrm{d}}{\mathrm{d}\tau}\mathbf{x}(t) \tag{6}$$

Therefore, having $\sigma = (\mathrm{d}\tau/\mathrm{d}t)^{-1}$, the normalized nonlinear dynamics are expressed by:

$$\frac{\mathrm{d}}{\mathrm{d}\tau}\mathbf{x}(\tau) = \sigma \cdot f(\mathbf{x}(\tau), \mathbf{u}(\tau)) \tag{7}$$

where $\sigma = t_f$ since $\tau \in [0, 1]$. Furthermore, for the sake of simplicity, aerodynamics are modeled as if the vehicle were subjected to a pure drag force. Assuming that the rocket is axisymmetric, the aerodynamic forces and moments in the vehicle's body-fixed reference frame are expressed by:

$$\begin{aligned} \mathbf{F}_{aero,B}(t) &= -\frac{1}{2}\rho(t)||\mathbf{v}_I(t)||_2 S_{ref} C_D(\alpha = \pi, M(t))\mathbf{R}_B^I(t)\mathbf{v}_I(t) \\ \mathbf{M}_{aero,B}(t) &= [\mathbf{x}_{CP} - \mathbf{x}_{CG}(t)] \times \mathbf{F}_{aero,B}(t) \end{aligned} \tag{8}$$

where $C_D(\alpha = \pi, M(t))$ is the actual drag coefficient, which is estimated from the available lookup tables. Note that, within the guidance, the velocity vector, $\mathbf{v}_I(t)$, does not account for wind.

Several state and control constraints are enforced in the optimization problem. Among the state constraints, we consider the lower bound of the mass, the so-called glide-slope constraint, the tilt angle constraint, the higher bound of the angular rate, and the preservation of the unit norm of the quaternions. Note that, in the latter case, the linearization was used for simplicity, but more advanced strategies can be implemented. For example, Ref. [37] describes the augmented convex–concave decomposition for this particular case. Finally, control constraints involve bounding the thrust direction and magnitude (higher and lower bounds). All the constraints in Figure 3 are thoroughly described in Ref. [26].

Due to the linearization process involved in the successive convex optimization strategy, trust regions and virtual controls are implemented to prevent unboundedness and artificial infeasibility, respectively. More particularly, trust regions limit the deviation between the two consecutive iterations responsible for artificial unboundedness. They are defined for the state and control vectors, as well as for the time of flight, and are penalized in the cost function. Virtual controls are additional control inputs that allow for reaching each point of the solution domain through dynamics relaxation and therefore avoid artificial infeasibility. Therefore, they are added in the linear discrete dynamics and then penalized in the cost function. The reader is referred to Ref. [26] for a better understanding of trust regions and virtual control implementation and their convexification through slack variables definition.

Finally, the cost function is defined as follows:

$$J = \sigma^i - m^i[K] + w_\nu S_\nu^i + w_{\boldsymbol{\Delta}_{\mathbf{x},\mathbf{u}}} S^i_{\boldsymbol{\Delta}_{\mathbf{x},\mathbf{u}}} + w_{\Delta_\sigma}\Delta_\sigma^i \tag{9}$$

where w_ν, $w_{\boldsymbol{\Delta}_{\mathbf{x},\mathbf{u}}}$, and w_{Δ_σ} are penalization weights, respectively penalizing the virtual controls, the trust region of the state and control vectors, and the trust region of the time of flight. Furthermore, S_ν^i and $S^i_{\boldsymbol{\Delta}_{\mathbf{x},\mathbf{u}}}$ are slack variables defined to avoid a quadratic term in the cost function. Whereas in Ref. [26] only the final mass ($-m^i[K]$) was considered to be maximized, this study also includes the minimum-time strategy through the parameter σ^i. In fact, due to the monotonic behavior of the propellant consumption with respect to time in this study and since the final time is also an optimization variable, the latter can also be selected as the value to be minimized. This choice leads to better performance when integrated in the closed-loop G&C simulator, as demonstrated in Section 5.

4. Structured H_∞ Control Synthesis

In this section, gain-scheduled structured H_∞ controllers are designed for the aerodynamic and powered descent phase of an RLV along a reference trajectory computed offline (corresponding to the first run of the guidance algorithm studied above) using the state-space representation described below. In fact, this control technique has been

demonstrated as a successful candidate in space applications to cope with the closed-loop requirements needed to enable robustness and performance [21,24,25]. In Ref. [38] from the same authors, gain-scheduled structured H_∞ controllers were already designed with the objective to recover a more basic control architecture. Even if the controllers obtained validated the control approach, more stability and robustness against uncertainties were needed. In this direction, a re-tuning of the controller gains is achieved in this study, also involving attitude rate and trajectory tracking (only Euler angle tracking previously). Tighter stability margins are considered, and a robustness analysis via structured singular value μ-analysis, which directly considers uncertainties in the linear RLV model, is included. More particularly, the requirements include closed-loop stability, attitude and trajectory tracking, and actuation limitation ($\beta_{TVC,i} \leq 10$ deg, $\beta_{fin,i} \leq 35$ deg) taken from Ref. [29], as well as stability margins (the gain margin must be superior to 6 dB and the phase margin must be superior to 30 deg). Note that the maximum actuator deflection considered in this paper is high (especially for the fins), and was selected for this analysis for simplicity, but at later design stages more realistic values should be integrated.

4.1. State-Space Representation of the RLV Descent Dynamics

Before proceeding with the linearization of the equations of motion, several assumptions must be made. First, the launch vehicle is considered axisymmetric with a negligible roll rate, therefore allowing for the decoupling of the motion in the pitch and yaw planes. Wind disturbances are not considered at this stage. Additionally, for the sake of simplicity, the effects of actuators, sensors, bending, and sloshing dynamics are ignored. Note that wind and all these features could be added in future work following the scheme available in the literature [24,39]. Concerning the neglect of bending modes, the reader is referred to Ref. [40], where relevant analyses have been carried out to ensure that their frequency is sufficiently larger than the closed-loop bandwidth of the controller. In this section, only the pitch dynamics will be defined for conciseness, but the expressions obtained for the yaw dynamics are available in Appendix A.3.

The pitch dynamics are described with the following state-space realization obtained by the linearization of the perturbed equations of motion translated in the vehicle's body fixed reference frame. Details of the linearization process are provided in Appendix A. Therefore, linearized perturbations are represented by the linear time invariant model G^{θ}_{RLV}, which is defined as:

$$\begin{bmatrix} \Delta\dot{\theta} & \Delta\ddot{\theta} & \Delta\dot{z}_B & \Delta\ddot{z}_B \end{bmatrix}^T = \mathbf{A}_\theta \begin{bmatrix} \Delta\theta & \Delta\dot{\theta} & \Delta z_B & \Delta\dot{z}_B \end{bmatrix}^T + \mathbf{B}_\theta \begin{bmatrix} \Delta\beta_{TVC,y} & \Delta\beta_{fin,y} \end{bmatrix}^T \tag{10}$$

where $\Delta\theta$, $\Delta\dot{\theta}$, and $\Delta\ddot{\theta}$ represent pitch angle perturbations and first/second-order derivatives and Δz_B, $\Delta\dot{z_B}$, and $\Delta\ddot{z_B}$ are the lateral drift and derivatives. The matrices $\mathbf{A}_\theta$ and $\mathbf{A}_\theta$ are defined by:

$$\mathbf{A}_\theta = \begin{bmatrix} 0 & 1 & 0 & 0 \\ 0 & 0 & 0 & \frac{\mu_{\alpha'}}{v_{x,0}} \\ 0 & 0 & 0 & 1 \\ -a_{0,\theta} & v_{x,0} & 0 & -\frac{N_{\alpha'}}{m \cdot v_{x,0}} \end{bmatrix}, \quad \mathbf{B}_\theta = \begin{bmatrix} 0 & 0 \\ -\mu_{TVC}\cos\beta_{TVC,y0} & -\mu_{fin,y,\gamma}\cos\beta_{fin,y0} \\ 0 & 0 \\ -\frac{T_{ref}}{m}\cos\beta_{TVC,y0} & \frac{N_{fin,y,\gamma}}{m}\cos\beta_{fin,y0} \end{bmatrix} \tag{11}$$

The terms in Equation (11) are defined in Appendix A.2.

Before synthesizing the control system, the assumption stating that the 6-DoF dynamics can be decoupled between the pitch and yaw planes is verified by eigenvalue analysis. More particularly, the poles of the 6-DoF decomposition, whose state-space representation is available in Appendix A.1 through Equation (A14), are computed and compared with the poles of G^{θ}_{RLV}, as well as its equivalent in the yaw plane (see Equations (A20)–(A22)). Figure 4 displays the poles of the decoupled systems (superposition of the poles of both systems, translating pitch and yaw dynamics) and the 6-DoF system for which the couplings have not been neglected.

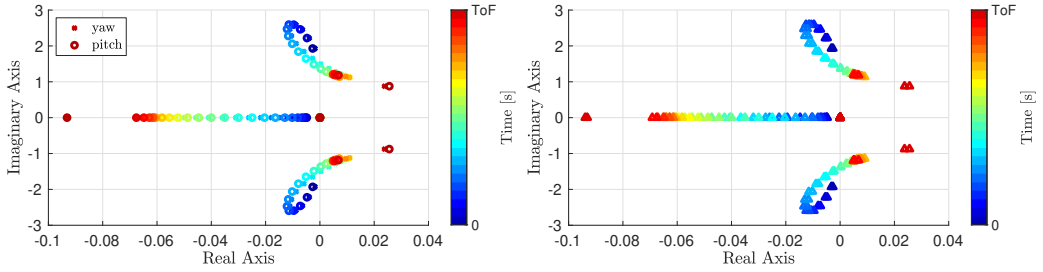

(**a**) Pitch and yaw linear models (**b**) Full 6-DoF linear model

Figure 4. Comparison of the eigenvalues of the decoupled systems with respect to those of the full 6-DoF state-space realization.

From this figure, we can observe that the eigenvalue distribution with respect to time is highly similar. More particularly, in Table 1 are reported the values of the poles for $t = 50.2$ s. As expected, the structure of the 6-DoF system is similar to the ones of the reduced model, and also the discrepancy between the yaw and pitch models is small due to the axial symmetry of the rocket.

Table 1. Eigenvalues for $t = 50.2$ s.

6-DoF System	Pitch System	Yaw System
$0.0000 + 0.0000i$	$0.0000 + 0.0000i$	$0.0000 + 0.0000i$
$0.0000 + 0.0000i$	$0.0069 + 1.1548i$	$0.0108 + 1.1315i$
$0.0000 + 0.0000i$	$0.0069 - 1.1548i$	$0.0108 - 1.1315i$
$0.0000 + 0.0000i$	$-0.0561 + 0.0000i$	$-0.0594 + 0.0000i$
$0.0086 + 1.1477i$		
$0.0086 - 1.1477i$		
$1.9244 \times 10^{-10} + 0.0000i$		
$-0.0598 + 0.0000i$		
$-0.0561 + 0.0000i$		
$0.0069 + 1.1548i$		
$0.0069 - 1.1548i$		
$0.0000 + 0.0000i$		

4.2. Structured H_∞ Control Problem Formulation

The system constituted by the RLV linear dynamics model developed previously is subjected to significant changes during the descent flight, mainly due to the variations associated with thrust and aerodynamics. In fact, Figure 5 shows as an example the Bode plot of the system G^{θ}_{RLV}, where the linear dynamics are discretized according to the altitude with $n = 15$ points. Therefore, it justifies the use of gain-scheduling to increase the performance and robustness of the control system.

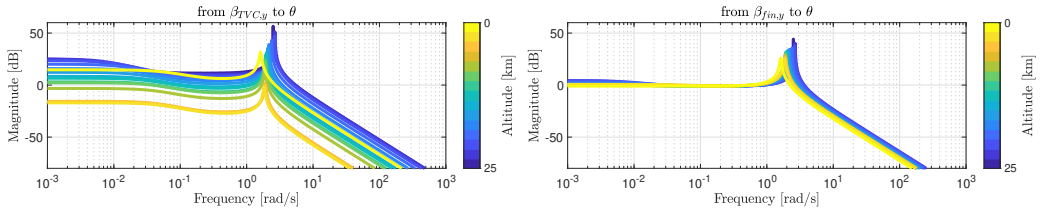

(**a**) From TVC to pitch angle (**b**) From fins to pitch angle

Figure 5. System transfer function with respect to altitude.

The altitude has been chosen as the scheduling parameter since it is monotonically evolving with respect to time and has been well validated in the literature [24,25]. The 15 points were equally distributed with respect to the altitude vector, which allows us to capture the variations well in terms of thrust magnitude and dynamic pressure.

In the framework of structured H_∞, the augmented plant must be defined. It is usually made up of the linear dynamics model of the system, the controller to be designed, other linear systems describing the effects of the actuators (TVC and fins) or disturbances such as wind, and a set of weights that include design specifications. Note that, in this study, for simplicity, the effects of sensors, actuators, and wind disturbances are not considered. A PID structure was used for the controllers designed in Ref. [38], taking the pitch angle error, θ_e, as input and giving the actuator deflections, $\{\beta_{TVC,y}, \beta_{fin,y}\}$, as outputs. In this work, attitude rate and trajectory tracking are also included for enhanced stability, so controllers take pitch angle, rate, and lateral body velocity errors $\{e_\theta, e_{\dot\theta}, e_{\dot z_B}\}$ as inputs and actuator deflections as outputs. Note that here the synthesis is depicted for the pitch dynamics, but the same methodology is followed for the yaw dynamics. Figure 6 shows the augmented plant named $M'(s)$.

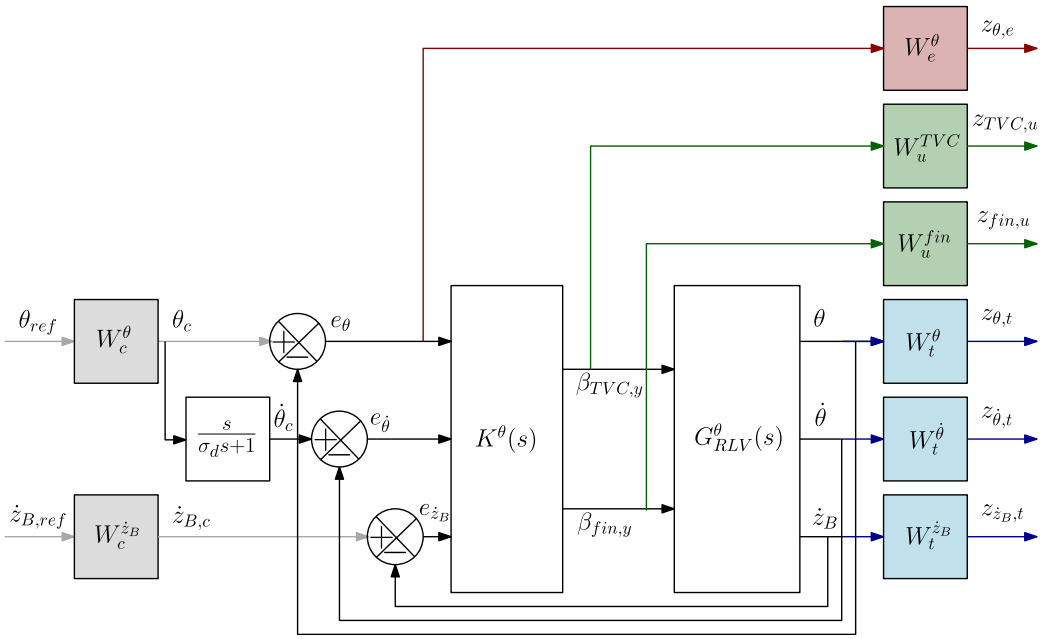

Figure 6. Pitch control augmented plant, $M'(s)$.

The exogenous inputs are the reference pitch angle, θ_{ref}, and lateral body velocity, $\dot z_{B,ref}$, scaled by the input weighting function $W_c = \text{blkdiag}\left[W_c^\theta \quad W_c^{\dot z_B}\right]$, which translates them into the signals θ_c and $\dot z_{B,c}$, respectively. The scaled pitch rate command, $\dot\theta_c$, is obtained using a first-order derivative filter with time constant $\sigma_d = 0.2$ s. The comparison of the scaled references $\{\theta_c, \dot\theta_c, \dot z_{B,c}\}$ and the outputs $\{\theta, \dot\theta, \dot z_B\}$ generates the errors $\{e_\theta, e_{\dot\theta}, e_{\dot z_B}\}$ entering the controller $K^\theta(s) = \left[K_{TVC}(s) \quad K_{fin}(s)\right]^T$. Then, the deflection angles $\{\beta_{TVC,y}, \beta_{fin,y}\}$ enter the RLV linear dynamics model. The mixed $T/S/KS$ sensitivity approach is employed for design tuning, where the output weighting functions $W_t = \text{blkdiag}\left[W_t^\theta \quad W_t^{\dot\theta} \quad W_t^{\dot z_B}\right]$, W_e^θ, and $W_u = \text{blkdiag}\left[W_u^{TVC} \quad W_u^{fin}\right]$ shape the tracking performance, the disturbance rejection capability, and the control efforts, respectively. More particularly, the controller is defined by:

$$\begin{aligned} K^\theta &= \left[K_{TVC} \quad K_{fin}\right]^T, \quad \text{where} \\ K_{TVC} &= \left(K^\theta_{p,TVC} + \frac{K^\theta_{i,TVC}}{s}\right) e_\theta + K^{\dot\theta}_{p,TVC} e_{\dot\theta} + K^{\dot z_B}_{p,TVC} e_{\dot z_B}, \\ K_{fin} &= \left(K^\theta_{p,fin} + \frac{K^\theta_{i,fin}}{s}\right) e_\theta + K^{\dot\theta}_{p,fin} e_{\dot\theta} + K^{\dot z_B}_{p,fin} e_{\dot z_B}. \end{aligned} \tag{12}$$

Therefore, the objective of the H_∞ optimal control problem is to find the gains $K^\theta_{p,TVC}$, $K^\theta_{i,TVC}$, $K^{\dot\theta}_{p,TVC}$, $K^{\dot z_B}_{p,TVC}$ and $K^\theta_{p,fin}$, $K^\theta_{i,fin}$, $K^{\dot\theta}_{p,fin}$, $K^{\dot z_B}_{p,fin}$, which constitute a stabilising controller, K^θ, such that the H_∞-norm of the augmented system is minimized. The optimal problem is defined by:

$$\min_{K^\theta_{p,TVC},K^\theta_{i,TVC},K^{\dot\theta}_{p,TVC},K^{\dot z_B}_{p,TVC},K^\theta_{p,fin},K^\theta_{i,fin},K^{\dot\theta}_{p,fin},K^{\dot z_B}_{p,fin}} ||M'_{\mathbf{w}\to\mathbf{z}}(s)||_\infty \tag{13}$$

where $\mathbf{w} = \begin{bmatrix}\theta_{ref} & \dot z_{B,ref}\end{bmatrix}^T$, $\mathbf{z} = \begin{bmatrix}z_{\theta,e} & \mathbf{z}_t & \mathbf{z}_u\end{bmatrix}^T$, with $\mathbf{z}_t = \begin{bmatrix}z_{\theta,t} & z_{\dot\theta,t} & z_{\dot z_B,t}\end{bmatrix}^T$ and $\mathbf{z}_u = \begin{bmatrix}z_{TVC,u} & z_{fin,u}\end{bmatrix}^T$. The non-smooth, non-convex optimization problem of Equation (13) is solved with `systune` since it enables one to directly include stability margin requirements through the command `TuningGoal.Margins`. Note that the chosen structural template and the actuation limitations result in H_∞-norm values that slightly exceed 1, depending on the altitude range. This behaviour is typical in rocket applications [24,41]. However, the overall tuning strategy effectively prevents the actuation system from reaching saturation, while also satisfying the mission requirements related to tracking and disturbance rejection, as described in the next subsections.

The command `TuningGoal.WeightedGain` is used to define the weighting functions. The input weighting function W_c, used for reference scaling, is determined based on the allowed maximum value for the input reference, here, the pitch angle and the lateral body velocity. For this study, we set:

$$\begin{aligned} W_c(s) &= \text{blkdiag}\begin{bmatrix}W_c^\theta & W_c^{\dot z_B}\end{bmatrix} \\ \text{where}\quad W_c^\theta(s) &= \frac{\pi}{180}\,\text{rad} \quad\text{and}\quad W_c^{\dot z_B}(s) = [1,2]\,\text{m/s}\end{aligned} \tag{14}$$

The output weighting functions W_t, W_e^θ, and W_u must complete the $T/S/KS$ mixed sensitivity synthesis problem. In fact, their inverse bound, respectively, the complementary sensitivity function, T, the sensitivity function, S, and the control sensitivity function, KS. Usually, $(W_e^\theta)^{-1}$ is chosen as a high-pass filter, whereas $(W_t)^{-1}$ and $(W_u)^{-1}$ are chosen as low-pass filters [21]. Therefore, the pitch angle error weighting function is defined as follows:

$$(W_e^\theta)^{-1}(s) = \frac{\pi}{180}\frac{h_e^\theta s + \omega_e^\theta}{s + \frac{\omega_e^\theta}{l_e^\theta}} \tag{15}$$

According to Refs. [25,41], the low-frequency attitude sensitivity is limited when controlling translational degrees of freedom; therefore, the parameter $l_e^\theta = 0.75$, supposed to reduce the steady-state tracking error, is chosen to be larger. Then, the high-frequency $h_e^\theta = 1.5$ to keep small the maximum peak of the sensitivity function, which is critical to ensure good stability margins. ω_e^θ is the desired bandwidth, varying according to the altitude range studied from 0.005 to 0.75 rad/s. Then, $(W_t)^{-1}$ is selected as:

$$\begin{aligned} (W_t)^{-1} &= \text{blkdiag}\begin{bmatrix}(W_t^\theta)^{-1} & (W_t^{\dot\theta})^{-1} & (W_t^{\dot z_B})^{-1}\end{bmatrix} \\ \text{where}\quad &\begin{cases} (W_t^\theta)^{-1}(s) = \dfrac{\pi}{180}\dfrac{h_t^\theta s + \omega_t^\theta}{s + \frac{\omega_t^\theta}{l_t^\theta}}, \\ (W_t^{\dot\theta})^{-1}(s) = 1\,\text{rad}, \\ (W_t^{\dot z_B})^{-1}(s) = [10,15]\,\text{m/s}. \end{cases}\end{aligned} \tag{16}$$

with $l_t^\theta = h_e^\theta$ to keep the fundamental relationship between complementary sensitivity and sensitivity functions and reduce the parameters to be tuned, while $h_t^\theta = 0.001$. The tracking bandwidth is set to $\omega_t^\theta = 20$ rad/s. Finally, the control input weighting function is here

used to impose signal limitations in order to prevent actuator saturation. They are set using constant weighting functions as follows:

$$\begin{aligned}(W_u)^{-1}(s) &= \text{blkdiag}\left[\left(W_u^{TVC}\right)^{-1}(s) \quad \left(W_u^{fin}\right)^{-1}(s)\right],\\ \left(W_u^{TVC}\right)^{-1}(s) &= \frac{\pi}{180}10 \text{ rad}, \quad \left(W_u^{fin}\right)^{-1}(s) = \frac{\pi}{180}35 \text{ rad}\end{aligned} \tag{17}$$

Note that the values of the control weighting functions have been adequately selected with the maximum actuator deflections to ensure that the actuators are not saturated during descent flight.

4.3. Linear Analysis of the Controllers

This analysis is necessary to validate the controllers obtained according to the requirements set previously. The latter are meant to be applicable to the nominal case for the classical linear analysis, while we will deal with a perturbed formulation through a robustness stability and performance analysis via μ-analysis in Section 4.4.

To study the robustness and performance of a system (plant + controller), it is usual to analyse the closed-loop transfer functions. Therefore, the frequency domain is analysed by looking at the sensitivity, complementary sensitivity, and control sensitivity functions. The corresponding bode plots are shown in Figure 7 with respect to the θ_{ref} channel, since the focus is on attitude tracking.

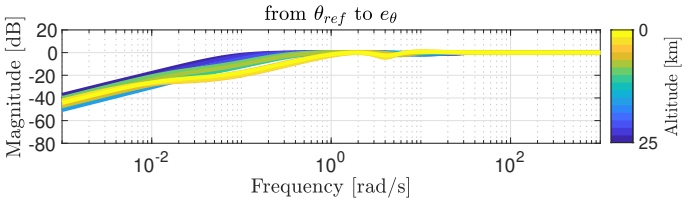

(**a**) Sensitivity function

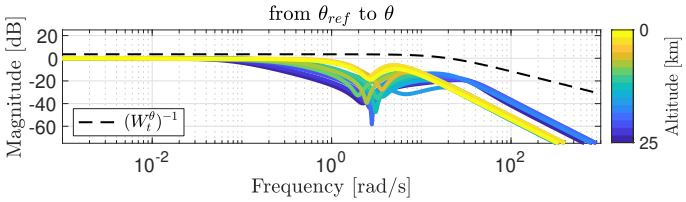

(**b**) Complementary sensitivity function

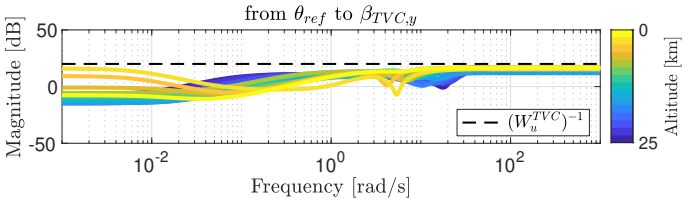

(**c**) TVC control sensitivity function

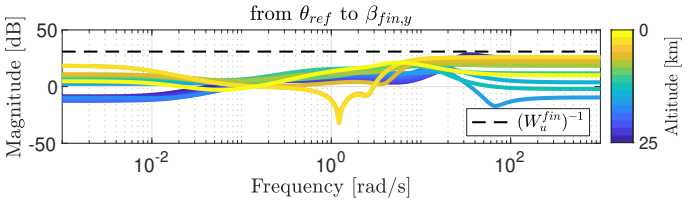

(**d**) Fin control sensitivity function

Figure 7. Frequency-domain linear analyses of the closed-loop system. The bound $(W_e^\theta)^{-1}$ is not shown since it is varying according to the altitude range studied, but all sensitivity functions are well below it.

The performance is quite good overall; the sensitivity function (Figure 7a) does not show peaks at low frequency, which is a good indicator for stability margins. Note that the sensitivity functions for all controllers are well below the corresponding weighting functions, $(W_e^\theta)^{-1}$, which validates the disturbance rejection requirement. The complementary sensitivity functions (Figure 7b) are well below the weighting function, $(W_t^\theta)^{-1}$, for all controllers, but there are some peaks that could represent a lack of stability. This will be checked in the next sections through robustness analysis and nonlinear simulations. Concerning the control sensitivity functions, shown in Figure 7c for the TVC system and in Figure 7d for the steerable planar fins, the requirements are also well met since the functions are below the weighting functions $\left(W_u^{TVC}\right)^{-1}$ and $\left(W_u^{fin}\right)^{-1}$, so saturation should be avoided. It is already possible to see that the last three altitude slots from orange to yellow show reduced performance.

Then, the time domain is also analysed by plotting the step response in Figure 8, again from the θ_{ref} channel.

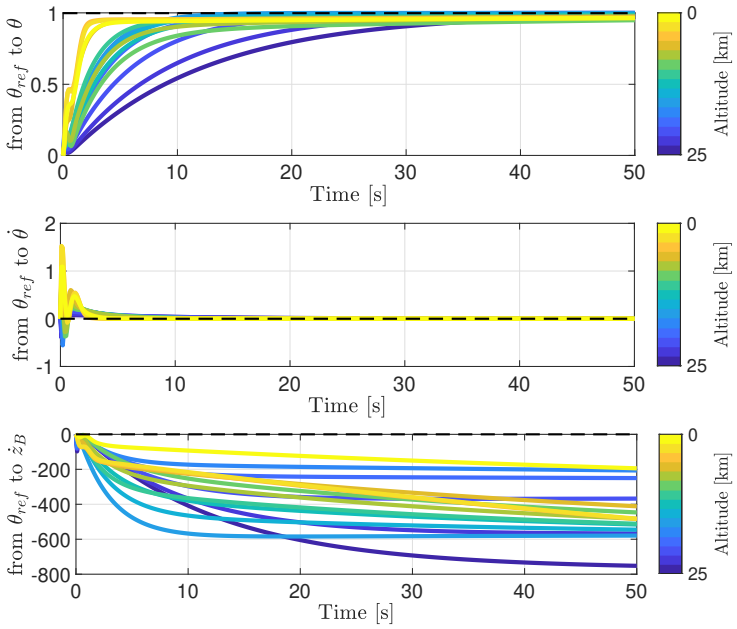

Figure 8. Step response for the synthesized control system from the θ_{ref} channel.

The dotted lines represent the steady-state values of the corresponding input–output pairs, which are desired to be 1 if associated with a command tracking or 0 in the case of disturbance. From this graph, we can observe good tracking capabilities without significant overshoot and with a relatively fast response in the θ_{ref} to θ channel. It is possible to see that the response is slower at the beginning of the flight and faster towards the end. This is related to the selected value of ω_e^θ for the weighting function that bounds the sensitivity function, $(W_e^\theta)^{-1}$. At the beginning of the flight, both the thrust magnitude and the dynamic pressure are high; therefore, high control capabilities are available. The stability margins are high, and an increased ω_e^θ was seen to reduce them. Consequently, because in this analysis we want to focus on increased stability and robustness to uncertainties, a settling time of 40–60 s was considered acceptable. However, towards the end of the flight, the dynamic pressure is decreased, leading to lower control capabilities, but the vehicle mass is also reduced, which increases the risk of instabilities. In this case, to obtain satisfactory results with respect to the requirements set, it was necessary to reduce the stability margins and improve the settling time of the step response (making it shorter). This is particularly the case for the last three sets of controller gains, which were already noticed as being less stable previously. Disturbances are well rejected with respect to the attitude rate, $\dot{\theta}$. However, the input lateral body velocity, $\dot{z}_{B,ref}$, was more difficult to control. This behaviour is observed because it was purposely decided not to tightly constrain the translational motion, since the focus was set on the attitude tracking. In the next sections, we will see the consequences of this choice on the vehicle's stability.

Figure 9 explicitly shows the stability margins obtained, with the gain margins on top and the phase margins below. Note that the Nichols charts have also been generated, but it was decided to directly display the stability margins for better readability. When a star is shown instead of a dot, it means that the gain margin is infinite. For the steerable planar fins, the gain margins are always above the requirement of 6 dB, with a minimum gain margin of 17 dB. However, for some altitude ranges, the phase margin is below the requirement of 30 deg, with a minimum phase margin of 23 deg. Nevertheless, the stability margin requirements are more difficult to satisfy for the TVC system, where a minimum gain margin of 3 dB is reached at 1.5 km altitude and with several phase margins below the requirement. We obtained a minimum phase margin of 6 deg at 2.1 km altitude. In fact, the requirement for the maximum deflection angle of the planar fins, $\beta_{fin,max} = 35$ deg, is not strict; therefore, no particular difficulty was observed to obtain the stability margins required. However, it was harder for the TVC system, first because the maximum

allowed gimbal angle, $\beta_{TVC,max} = 10$ deg, is lower but also because of the definition of the actuation system itself, which is less stable due to its similarity to an inverted pendulum. Consequently, small stability margins are noticed at the beginning of the flight, which is more likely related to the high thrust magnitude at this stage. Moreover, this behaviour can also be seen at the end of the flight since the thrust magnitude becomes high again and the vehicle mass is significantly reduced. It is particularly important to mention how critical this phase is since the fins' effectiveness is significantly reduced due to low dynamic pressure. In the controller gain tuning, it was not possible to improve these margins without significantly increasing the settling time of the step response of the closed-loop system. Therefore, we decided to conserve these gains and assess them through robustness analysis and nonlinear simulations in the following sections. Note that, in future works, the aerodynamic and powered descent phases should be separated with control systems that are properly designed for each phase in order to increase robustness.

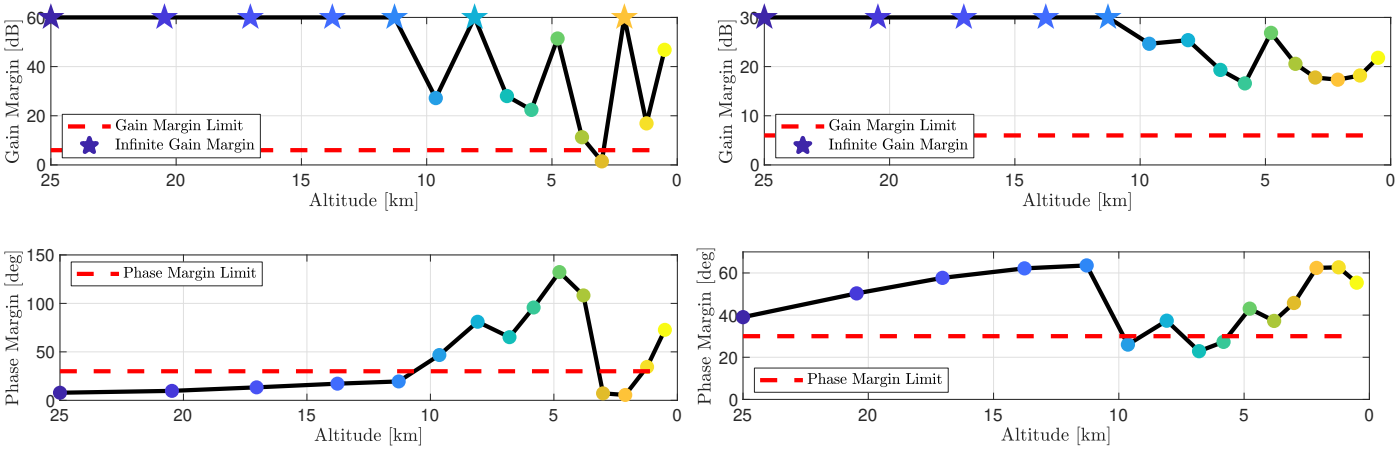

(**a**) $\beta_{TVC,y}$ to $\beta_{TVC,y}$ channel. (**b**) $\beta_{fin,y}$ to $\beta_{fin,y}$ channel.

Figure 9. Stability margins.

4.4. Robust Stability and Performance Analysis

The classical stability margins that come from the control design were quantified in the previous section. However, nothing was said about the robust stability and performance of such a design in the presence of uncertainties. In fact, the LFTs can be exploited to inject several uncertainties into the design. Specifically, the uncertainties and perturbations considered and gathered in the uncertainty block Δ are summarized in Table 2.

Table 2. Perturbations included through LFT for μ-analysis, taken from [22].

Perturbation	Variable	Value (%)
Normal RLV force gradient	$C_{N,LV\backslash\alpha}$	20
Normal fin force gradient	$C_{N,fin\backslash\gamma}$	20
Dynamic pressure	Q	20
CG position	x_{CG}	2
CP position	x_{CP}	10
Total RLV mass	m	2
Normal RLV MoI	J_N	2
Normal thrust force	$T_{ref}\cos(\beta_{TVC,y0})$	10
Longitudinal velocity	$V\cos(\alpha_0)$	10
Trim acceleration	a_0	10

These perturbations are included by the command `ureal` in MATLAB; they can be interpreted as multiplicative perturbations with a uniformly distributed multiplicative factor. Perturbations in forces and torques are considered through variations in mass,

dynamic pressure, and moments of inertia, as well as the corresponding coefficients. Furthermore, uncertainties have also been induced through the positions CG and CP, again affecting the torques generated. Finally, errors in estimated speed and acceleration are also considered. Note that the controller gains could also be tuned, accounting for these possible uncertainties, as was performed in Ref. [21]. However, in this study, the uncertainties are included through block Δ only to assess the robustness stability and performance of the previously synthesized gains [24,39].

With these uncertainties inserted in the nominal plant, the robustness of the designed system can now be assessed using the tools provided by the analysis of the structural singular value (μ-analysis) by inserting these uncertainties into the nominal plant. More particularly, this is done by reshaping the system in the classical $M-\Delta$ format, with Δ embedding all the uncertainties defined in Table 2 in a diagonal matrix and $M(s)$ representing the deterministic part of the augmented closed-loop system defined in Figure 6. Figure 10 describes the robust standard H_∞ interconnection augmented with the uncertainty blocks. Note that, in this configuration, the tunable controller $K^\theta(s)$ is removed from the generalised plant $P(s)$, with $\mathbf{u} = \begin{bmatrix}\beta_{TVC,y} & \beta_{fin,y}\end{bmatrix}^T$ representing the controller output and $\mathbf{y} = \begin{bmatrix}e_\theta & e_{\dot{\theta}} & e_{\dot{z}_B}\end{bmatrix}^T$ the controller input.

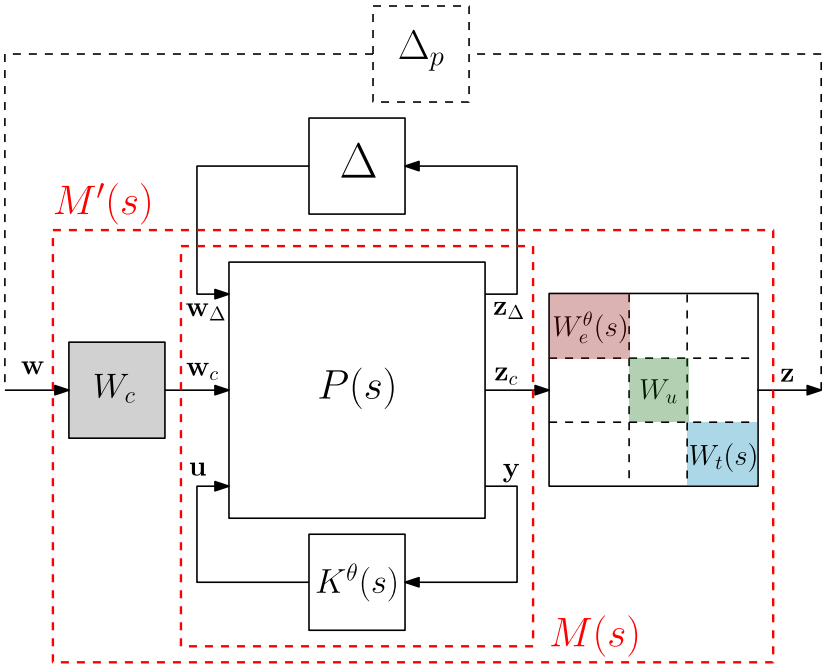

Figure 10. Augmented robust standard H_∞ interconnection for robust stability and performance analyses.

The structural singular value, μ, is usually defined as follows [42]:

$$\mu(M_{11}) = \frac{1}{\min_\Delta\{\bar{\sigma} : ||\Delta||_\infty \leq 1, \det(\mathbb{I} - M_{11}\Delta) = 0\}} \tag{18}$$

where M_{11} represents the transfer function from the uncertainty channel $\mathbf{w}_\Delta$ to $\mathbf{z}_\Delta$. Then, Robust Stability (RS) is ensured by the following criterion:

$$\mu(M_{11}(j\omega)) < 1, \quad \forall\omega \in \mathbb{R} \tag{19}$$

Furthermore, the structured singular value can also be used for Robust Performance (RP) analysis. In that context, the robust interconnection of Figure 10, including the weighting functions and denoted as $M'(s)$, is closed using a fictitious full-complex perturbation

matrix, Δ_p, which does not represent any actual perturbation of the system. The RP criterion is then defined as follows [43]:

$$\mu(M'(j\omega)) < 1, \quad \forall \omega \in \mathbb{R} \tag{20}$$

For both, instead of μ directly, we estimate their upper and lower bounds for the system under analysis. Therefore, when these bounds are close to each other, they uniquely identify the real μ value of the system. These analyses are achieved using the MATLAB tools `robstab`, for robust stability, and `robgain`, for robust performance.

First, Figure 11 shows the results of the robust stability analysis. On the top in Figure 11a, the upper bounds (in solid lines) and the lower bounds (in dashed lines) are represented for all linear design points. On the bottom in Figure 11b, the sensitivities associated with each parameter of Table 2 are highlighted for the linear design point at $h = 2110$ m, which corresponds to the worst-case point in terms of controllability. The μ bounds for this specific case are repeated at the top to better facilitate the analysis.

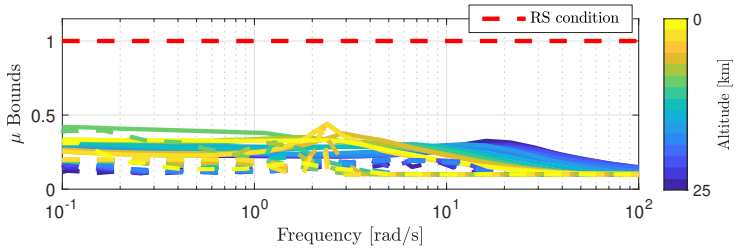

(**a**) μ bounds for all design points.

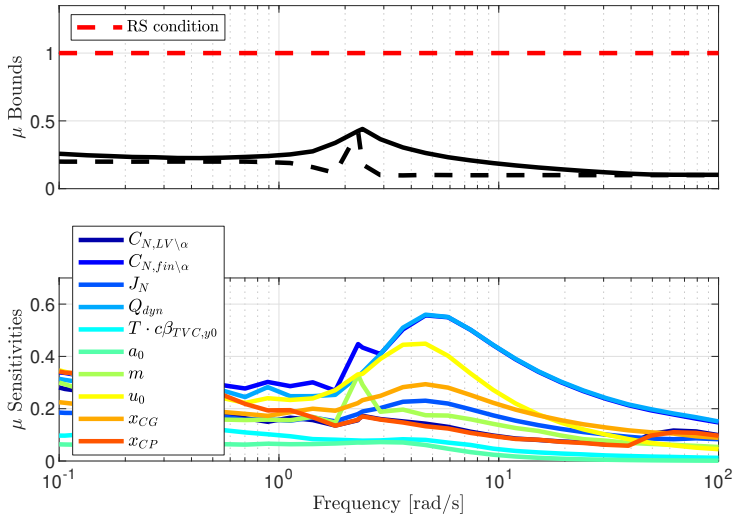

(**b**) Sensitivities at $h = 2110$ m.

Figure 11. Robust stability analysis with the sensitivities associated with each parameter at a prescribed altitude. Upper bounds are represented in solid lines and lower bounds in dashed lines.

From Figure 11a, we can see that the bounds are well below 1, therefore ensuring a good robust stability against uncertainties. It can be observed that, at high altitudes, the controller gains generated larger bounds at a relatively high frequency (around 13 rad/s), whereas it is the opposite at lower altitudes. In the linear analysis of the previous section, it was noticed that the last three altitude slots from orange to yellow were more difficult to manage. The observed reduced performance is confirmed by looking at the μ-bound peaks obtained in Figure 11a at a frequency of 2.4 rad/s. However, these bounds remain largely below 1, so the robustness stability of the controllers is satisfied for the uncertainties considered. From the sensitivities in Figure 11b, it can be noticed that the normal force gradient of the fin, $C_{N,fin\backslash\gamma}$, and the dynamic pressure, Q, are the main causes of degradation at

$h = 2110$ m due to the large control authority that fins have compared to the TVC system. Moreover, the μ-bound peak corresponds to a peak of the μ sensitivities of the normal force gradient of the fin, $C_{N,fin\backslash\gamma}$, and the mass, m. In fact, at low altitude, the vehicle is light since most of the propellant has been consumed, and consequently any movement of the fins, even slight, significantly affects its behaviour .

Figure 12 on the bottom left shows the results of the robust performance analysis. Note that the lower bounds are omitted for ease of readability. From this figure, it is possible to notice that the robust performance criterion is not met since, for some frequencies, the μ upper bound is bigger than 1. However, this result is still interesting to understand the key factors that lead to poorer performance. In these cases, we observe a peak above 1 at 30 rad/s for the linear design point at $h = 25$ km as well as three peaks around 2–4 rad/s, corresponding to the linear design points at low altitude (from 2110 to 0 m). For the latter, they are more likely due to a lack of controllability, since the dynamic pressure and thrust power available are low (due to the small propellant mass remaining). Concerning the peak at 25 km altitude, it is more likely due to a lack of controllability of the TVC system at the starting point of the simulation.

To conclude this section, the robustness analysis and the performance of the gains from the synthesized rigid body controllers through μ-analysis were satisfactory, as only lack of performance was observed, which is common for launcher control system design [21,24]. The latter is particularly noticed at low altitude and correlated with low stability margins. For the study carried out in this paper, the control system obtained is sufficient, but for future developments this lack of robustness should be corrected since the integration of delays and actuator models on the nonlinear simulator would significantly increase the risk of instability.

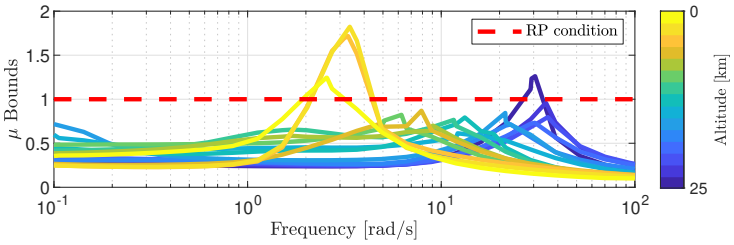

Figure 12. Robust performance analysis.

5. Closed-Loop 6-DoF Nonlinear Simulations

Once the gains of the controllers are synthesized and assessed through linear analysis, the next step is to verify that the control strategy is effective in controlling the real plant in the 6-DoF nonlinear, closed-loop environment, not only for nominal conditions but also in the presence of uncertainties and disturbances. In that context, the controlled dynamics simulator described in Section 2 is used in closed-loop with the guidance algorithm of Section 3 and the control system synthesized in Section 4. Note that, in the simulator, the guidance algorithm directly provides the thrust magnitude and only the directions result from the control system. This approximation is penalized by a low-pass filter, which simulates the intrinsic physics of the engine, and the delay induced is compensated for by a PI controller [26]. For simplicity, no engine rate limitation is assumed. Moreover, a lower bound of 0 kN is considered to enable a "switch-off" mode of the main engine. Note that the latter is an unrealistic assumption in practice. The initial and final conditions defined in Table 3 are assumed. Note that the scenario studied in this paper consists of one single phase combining TVC and aerodynamic steering. It illustrates the descent and precise landing of a reusable rocket and considers that the boostback manoeuvrer, re-entry burn, and a part of the aerodynamic descent are already achieved, which explains why the starting altitude is 25 km. For simplicity, the main engine is kept on for the entire flight duration, even if the lower bound of the thrust magnitude in the guidance algorithm could allow for zero thrust. The performance results are therefore compared with those obtained

in Ref. [26] with a simpler G&C system. The purpose of this analysis is to show the benefits of robust H_∞ control theory compared to a classical control system. Furthermore, it is shown that this technique can be coupled with several cost function strategies within the advanced guidance algorithm, allowing the best performing solution to be selected.

Table 3. Initial and final conditions.

State	Value	State	Value
$\mathbf{r}_I[0]$	$[25 \;\; 0 \;\; -15]^T$ km	$\mathbf{r}_I[K]$	$[0 \;\; 0 \;\; 0]^T$ m
$\mathbf{v}_I[0]$	$[-850 \;\; 0 \;\; 950]^T$ m/s	$\mathbf{v}_I[K]$	$[-5 \;\; 0 \;\; 0]^T$ m/s
$\boldsymbol{\omega}_B[0]$	$[0 \;\; 0 \;\; 0]^T$ rad/s	$\boldsymbol{\omega}_B[K]$	$[0 \;\; 0 \;\; 0]^T$ rad/s
$m[0]$	14,000 kg	$\mathbf{q}_B^I[K]$	$[0 \;\; 0 \;\; 0 \;\; 1]^T$

Section 5.1 shows the results of the nominal simulations. Then, the impact of disturbances and uncertainties through Monte-Carlo analysis is studied in Section 5.2.

5.1. Nominal Conditions

For this study, no wind was considered and, for simplicity, neither propellant sloshing effects nor flexible bending modes were included. Note that these effects are easily implementable within the present simulator, which could therefore constitute a relevant tool for such analyses [40]. Figure 13 shows the results of the nonlinear simulation and compares it with the G&C system used in Ref. [26], involving a classical linear control theory and maximum-final-mass cost function strategy in the guidance logic, here denoted as J_{m_f}. Recall that the G&C system developed in this paper, here denoted as $H_\infty / J_{t_f - m_f}$, combines robust structured H_∞ control with a guidance algorithm that optimizes the time of flight and the vehicle final mass. Table 4 summarizes the performance results of both systems in terms of final mass, m_f, final downrange position, D_f, final velocity, v_f, and time of flight, ToF.

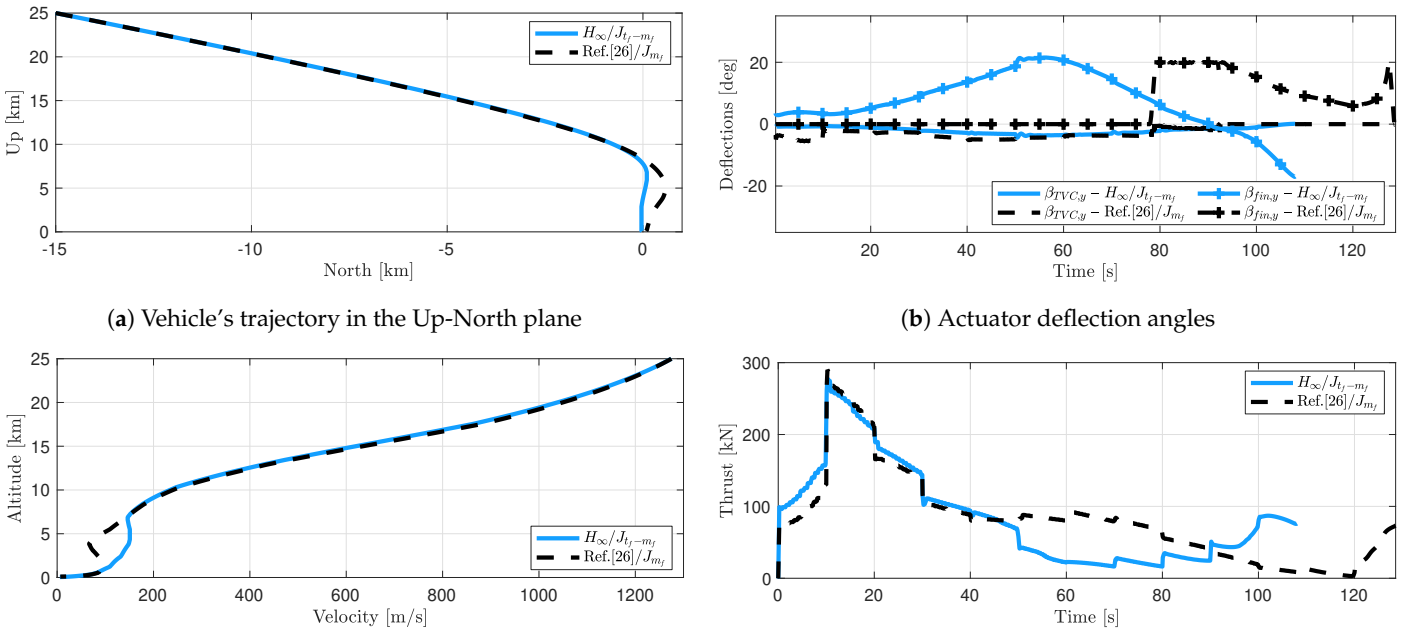

(**a**) Vehicle's trajectory in the Up-North plane

(**b**) Actuator deflection angles

(**c**) Altitude versus velocity.

(**d**) Thrust magnitude profile

Figure 13. Nominal trajectory simulation within the nonlinear controlled dynamics simulator. In black dashed lines are represented the results obtained using the G&C system of Ref. [26].

Table 4. Performance results for the different G&C systems.

	$H_\infty/J_{t_f-m_f}$	Ref. [26]/J_{m_f}
Final mass ($m_f > 2750$ kg)	4583 kg	2767 kg
Final downrange ($D_f = 0$)	26 m	84 m
Final velocity ($v_f = 5$ m/s)	5.64 m/s	6.53 m/s
Time of flight *ToF*	108 s	129 s

Figure 13a,c show that the obtained trajectories from the nonlinear simulations of both systems are significantly different. While the one of Ref. [26] overshot the landing site and then came back to it, the new trajectory represented in blue solid lines reduces the velocity of the vehicle until precise touchdown. This is due to better management of the available control authorities, since the new G&C system can combine TVC and planar fin steering, while in Ref. [26] both actuators were used alternatively according to the thrust magnitude and only associated when the primary system was saturated. This can be observed in Figure 13b; while for Ref. [26] only TVC is used until 80 s of flight (since the commanded thrust magnitude is kept high), the structured H_∞ control system coupled with the $J_{t_f-m_f}$ cost function combines the actuator action, which therefore generates a faster descent flight while still satisfying the strict accuracy requirements. Figure 13d shows the evolution of the thrust magnitude during the descent flight. It is possible to notice that both profiles are similar until 50 s of flight, where the thrust magnitude generated by the $H_\infty/J_{t_f-m_f}$ system starts to decrease. This behaviour leads to the shift in vehicle velocity observable in Figure 13c, where we see that the velocity is no longer linearly decreasing with respect to the altitude. As a consequence, the vehicle reache the landing site more rapidly and with the desired velocity thanks to the increase of the commanded thrust magnitude in the last ten seconds of flight. By looking at Table 4, we can directly conclude that these changes are beneficial; the thrust magnitude profile generated by the guidance algorithm enables a non-negligible increase of the vehicle final mass (1816 kg are saved compared to Ref. [26]), therefore ensuring the safety of the launcher recovery while allowing room for a heavier payload. Furthermore, the final downrange position and final velocity are also improved for the $H_\infty/J_{t_f-m_f}$ system compared to the one of Ref. [26]. To conclude, the enhancements of the G&C system for launcher descent and precise landing proposed in this paper through robust structured H_∞ control and advanced guidance strategy show a significant increase in performance: the multivariable control system enables a good management of the available control authorities and can be efficiently coupled with an advanced guidance algorithm, optimizing the fuel consumption while ensuring a precise landing. However, the results also highlight the room for improvements. In fact, in the present control strategy, no feedback on horizontal position components are considered to keep consistency with Ref. [26]. This therefore explains the final downrange errors. For better performance, feedback on the downrange could therefore be included in the control synthesis strategy, as in Ref. [24], and the tracking of the lateral body velocity should be reinforced. Similarly, it could be relevant to include the altitude and the altitude rate in the state-space representation to enable a better management of the TVC system.

To better understand the choice of the cost function, several strategies are assessed for the nominal conditions within the nonlinear controlled dynamics simulator in closed-loop with the structured H_∞ control system. It includes $J_{t_f-m_f}$ = Equation (9), as well as the following cost functions:

$$J_{t_f} = \sigma^i + w_{\boldsymbol{\nu}} S^i_{\boldsymbol{\nu}} + w_{\boldsymbol{\Delta}_{\mathbf{x},\mathbf{u}}} S^i_{\boldsymbol{\Delta}_{\mathbf{x},\mathbf{u}}} + w_{\Delta_\sigma} \Delta^i_\sigma \tag{21}$$

minimizing the final time of flight, and

$$J_{m_f} = -m^i[K] + w_{\boldsymbol{\nu}} S^i_{\boldsymbol{\nu}} + w_{\boldsymbol{\Delta}_{\mathbf{x},\mathbf{u}}} S^i_{\boldsymbol{\Delta}_{\mathbf{x},\mathbf{u}}} + w_{\Delta_\sigma} \Delta^i_\sigma \tag{22}$$

minimizing the final mass. Note that, for each cost function, the controller gains have been re-tuned following the same strategy described in the Section 4. The performance results are available in Table 5, where those of the $H_\infty/J_{t_f-m_f}$ system are repeated.

Table 5. Comparison of the performance results of several cost function strategies through nonlinear, closed-loop simulations.

	m_f	D_f	v_f	*ToF*
$H_\infty/J_{t_f-m_f}$	4583 kg	26 m	5.64 m/s	108 s
H_∞/J_{t_f}	3409 kg	21 m	5.25 m/s	119 s
H_∞/J_{m_f}	2768 kg	114 m	4.46 m/s	126 s

As mentioned in Section 3.2, the selected cost function, $J_{t_f-m_f}$, combining the minimization of the time of flight with the maximization of the final mass, enables the best optimization of the fuel consumption. We can notice a saving of 1174 kg compared to the second-best cost function strategy, J_{t_f}. To better understand these results, Figure 14 shows the thrust magnitude profiles obtained using different cost function strategies within the nonlinear simulator, as well as how the open-loop guidance reference profiles generated every 10 s are managed by the simulator.

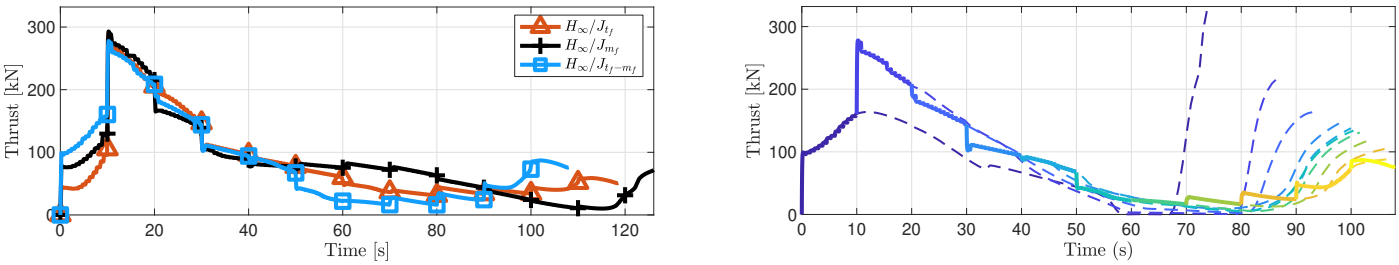

(**a**) Closed-loop thrust magnitude profiles comparison. (**b**) Corresponding open-loop guidance profiles of $H_\infty/J_{t_f-m_f}$.

Figure 14. Thrust magnitude profiles generated during the nonlinear, closed-loop simulations. On the left, the closed-loop thrust profiles of different cost function strategies are represented. On the right, the closed-loop $H_\infty/J_{t_f-m_f}$ thrust profile is represented in solid lines with its corresponding open-loop references, which are generated every 10 s by the guidance algorithm.

It can be seen in Figure 14a that $H_\infty/J_{t_f-m_f}$ generates the profile with the lowest thrust magnitude in the middle of the descent flight, between 50 and 90 s. In fact, the reduction of the thrust magnitude commanded allows for reaching the landing site more rapidly, therefore saving propellant, and before touchdown a more important burn is generated to decrease the vehicle velocity until the desired value. Note that aerodynamic steering is used efficiently during this phase, where the TVC system has reduced control authority. H_∞/J_{t_f} also generates a thrust magnitude profile that allows saving propellant; however, the reduction of thrust in the middle of the flight and the last burn are slightly lower compared to $H_\infty/J_{t_f-m_f}$, leading to a longer flight and therefore a reduced vehicle final mass. It seems that optimizing the time of flight alone generates a fast trajectory profile, which is more likely to be more aggressive with respect to the control commands needed (remember that only the thrust vector is considered as input) and consequently not totally achievable by the actual actuation system. As a result, the desired conditions are not reached and a new guidance computation must be executed, which paradoxically increases the simulation time. Combining this strategy with the maximum-final-mass allows one to reduce the thrust usage and to increase the velocity, which, when integrated in the closed-loop, enables one to reach the landing site faster with the benefit of using less propellant. Finally, maximizing the final mass alone through J_{m_f} generates a long flight that paradoxically significantly increases the fuel consumption. Once again, this result highlights the importance of assessing the guidance algorithm through nonlinear, closed-

loop simulations. This statement can be better understood with Figure 14b, where the open-loop reference thrust profiles generated by the guidance for the $H_\infty / J_{t_f - m_f}$ nonlinear simulation are depicted. Here, since the guidance algorithm is re-executed every 10 s, it cannot globally minimize the fuel consumption without memory of the propellant used in the previous iterations. For closed-loop simulations, when the time of flight is an optimization variable and is not specified by the user, it is therefore relevant to include it in the cost function for increased performance results.

5.2. Monte-Carlo Analysis

Finally, the structured H_∞ control system is tested through nonlinear simulations in the presence of disturbances and uncertainties to assess its robustness. The latter is once again compared to the control system developed in Ref. [26]. Therefore, the same dispersions are included in the simulator and 100 runs are performed. They are repeated in Table 6, where the symbols $\mathcal{U}$ and $\mathcal{N}$ refer to uniformly and normally distributed variables, respectively.

Table 6. Perturbations considered for the Monte-Carlo analysis.

Perturbation	Variable	Value
Initial lateral velocity	$v_z[0]$	$\sigma = 20$ m/s ($\mathcal{N}$)
Initial mass	$m[0]$	2 % ($\mathcal{U}$)
Moments of inertia	$J_A(t)$, $J_N(t)$	2 % ($\mathcal{U}$)
Reference thrust	$T_{ref}(t)$	10 % ($\mathcal{U}$)
Atmospheric density	$\rho(t)$	20 % ($\mathcal{U}$)
Ambient pressure	$P_{amb}(t)$	10 % ($\mathcal{U}$)
Drag coefficient	$C_D(t)$	20 % ($\mathcal{U}$)
Lift coefficient	$C_L(t)$	20 % ($\mathcal{U}$)

To better analyse the increase in robustness made possible by the use of the structured H_∞ control method compared to the baseline control of Ref. [26], we sorted the Monte-Carlo runs into three categories:

- *Not converged*: Convergence issue coming from the guidance algorithm or final altitude too high ($h_{ToF} > 500$ m), which therefore prevent the exploitation of the solution. Cases having a final mass lower than the dry mass of the vehicle ($m_{dry} = 2750$ kg) have also been added to this category because they are more likely to cause failure.
- *Safe*: Cases in which the final conditions are satisfactory for obtaining a soft pinpoint landing. In particular, the downrange error is less than 300 m and the final velocity is less than 10 m/s (note that the targeted final velocity is 5 m/s).
- *Unsafe*: All other cases. The latter are still feasible but do not present satisfying conditions for a precise soft landing.

Therefore, the Monte-Carlo solution sets sorted for both control strategies, the augmented structured H_∞, and the baseline, are compared. Figure 15 displays the results of this comparison, showing on the top from left to right the final mass, downrange error, and final velocity of the simulations obtained using robust H_∞, and on the bottom the same parameters for the simulation obtained using the baseline controller of Ref. [26]. Table 7 allocates the simulation runs in their corresponding categories for both G&C systems.

Table 7. Results of the 100-run Monte-Carlo analysis and comparison with the G&C system of Ref. [26].

	Not Converged	***Safe***	***Unsafe***
$H_\infty / J_{t_f - m_f}$	1	66	33
Ref. [26]/ J_{m_f}	41	34	25

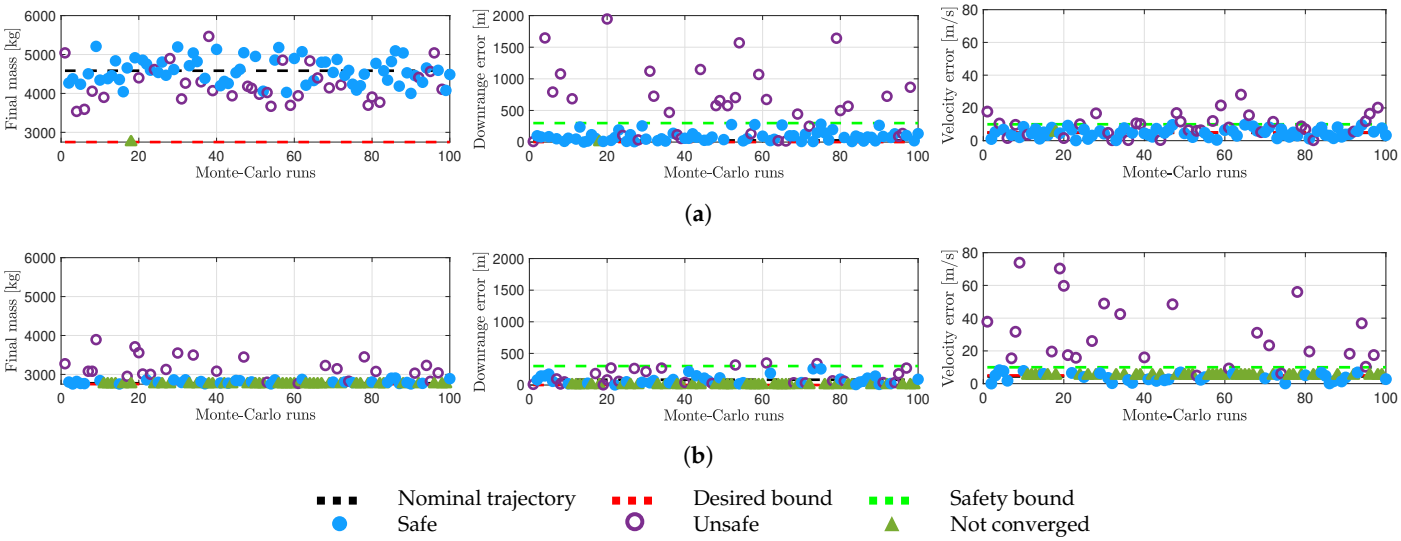

Figure 15. Comparison of the Monte-Carlo analyses. (**a**) 100-run Monte-Carlo analysis of the $H_\infty / J_{t_f - m_f}$ system. (**b**) 100-run Monte-Carlo analysis of the Ref. [26] / J_{m_f} system.

From this analysis, we can definitely observe that the structured H_∞ control method performs better in counteracting uncertainties and disturbances. In fact, of the 100 runs carried out only 1 failed due to a convergence issue of the guidance algorithm or due to a too-low final mass. In comparison, using the baseline controller, it occurred in 41 cases, most of the time due to the mass. Then, after removing failures, most of the remaining cases with the H_∞ control entered the previously defined category *safe*, therefore allowing a soft and precise landing of the launcher; 66% of the cases are *safe* while 33% are *unsafe*. In contrast, with the baseline control system, many cases were *unsafe* (25%), and only 34% of the runs performed entered the category *safe*. Therefore, this confirms the high robustness capability of the structured H_∞ control method compared to the classical one to counteract uncertainties and disturbances existing in the launcher environment. It is noticeable that, for this control strategy, the downrange error criterion is the one that leads most cases to the category *unsafe*. Therefore, a good addition to the strategy employed could be to directly track the downrange within the controller as in Ref. [24]. Similarly, the final velocity errors observable in many cases that are *unsafe* are directly correlated to the disturbance rejection capability of the control system with respect to the lateral body velocity analysed in Figure 8 of Section 4.3. This therefore confirms the need to reinforce translational tracking, which should also increase the stability margins and therefore the robustness of the control system. For the baseline control system, it is the mass that is the most critical, followed by the velocity error, therefore showing that this control design is less flexible to changes in the parameters.

6. Conclusions

In Ref. [26], a 6-DoF nonlinear controlled dynamics simulator for the aerodynamic powered descent and precise landing of reusable launchers was developed to assess G&C systems. As the baseline system for preliminary performance assessment, it involves a successive convex optimization algorithm, maximizing the vehicle final mass and a control system for which the MIMO formulation induced by the coupling of TVC and steerable planar fins was simplified to a series of SISO systems to apply classical linear control theory. The present paper is a follow up of that work, where the improvements are twofold: First, more robust gain-scheduled PID controllers are synthesized via the structured H_∞ method. The latter enables the proper combination of both actuators. Then, the assessment of the performance of the integrated G&C design enables the selection of a better cost function strategy.

In fact, the successive convex optimization algorithm implemented into the guidance system offers a modular architecture, enabling several cost function strategies to be evaluated. Among these, optimizing both the time of flight and the vehicle final mass increases the performance of the system. Furthermore, the structured H_∞ method enables one to directly consider the MIMO formulation, which means that the actuation corrections through TVC and planar fin deflections are optimized simultaneously throughout the descent flight. The robust framework associated with the structured H_∞ method allows one to directly consider control requirements when tuning the scheduled controllers. In addition, the control architecture for synthesis can be augmented with parametric uncertainty via LFT modelling. This asset enables a direct assessment of the robustness to uncertainties of the controllers obtained via μ-analysis without the need to use an extensive Monte-Carlo analysis campaign.

It is shown that such a G&C system, when assessed through closed-loop nonlinear simulations with the 6-DoF controlled dynamics simulator, provides significantly improved launcher performance and robustness to uncertainties and disturbances with respect to the baseline system developed in Ref. [26]. More particularly, a propellant mass saving of 1816 kg is performed while still ensuring a precise and soft landing of the reusable launcher.

The overall results show that the proposed G&C system represents a relevant candidate realistic descent flight and precise landing phase for reusable launch vehicles.

Author Contributions: Conceptualization, A.D.O.; methodology, A.D.O.; software, A.D.O.; validation, A.D.O.; formal analysis, A.D.O.; investigation, A.D.O.; resources, A.D.O.; data curation, A.D.O.; writing—original draft preparation, A.D.O.; writing—review and editing, A.D.O.; visualization, A.D.O.; supervision, M.L.; project administration, M.L.; funding acquisition, M.L. All authors have read and agreed to the published version of the manuscript.

Funding: The project leading to this application has received funding from the European Union's Horizon 2020 research and innovation programme under the Marie Sklodowska-Curie grant agreement No 860956. It is part of the ASCenSIon project, an Innovative Training Network (ITN) to advance space access capabilities (https://ascension-itn.eu/, accessed on 1 September 2024).

Data Availability Statement: No new data were created or analyzed in this study. Data sharing is not applicable to this article.

Conflicts of Interest: The authors declare no conflicts of interest.

Abbreviations

The following abbreviations are used in this manuscript:

6-DoF	Six-Degree-of-Freedom
CG	Center of Gravity
CP	Center of Pressure
D&L	Descent and Landing
G&C	Guidance and Control
GNC	Guidance, Navigation, Control
LPV	Linear Parameter Varying
LTV	Linear-Time-Varying
MIMO	Multiple-Input Multiple-Output
PID	Proportional-Integral-Derivative
RCS	Reaction Control System
RLV	Reusable Launch Vehicle
SISO	Single-Input Single-Output
SOCP	Second-Order Cone Programming
STC	State-Triggered Constraint
TVC	Thrust Vector Control
VTVL	Vertical Take-Off Vertical Landing

Appendix A. Derivation of State-Space Models

In this appendix, details for the derivation of the state-space models used in Section 4.1 are provided, together with the assumptions considered. While, in the literature, the use of TVC-only for launcher ascent and descent flight control has been well addressed [44,45], Ref. [46] derived a general linear representation of RLV dynamics in ascent and descent flights with a combined use of TVC and fins. This linear representation of the flight dynamics was adapted to the problem considered in this paper, and the outcomes are developed hereafter. Another state-space representation for the launcher aerodynamic descent phase (unpowered) can be found in Ref. [24].

The 6-DoF equations of motion, available in Equations (2) and (3), are formulated in the vehicle's body-fixed reference frame, whose the kinematics are expressed through the Euler angles formulation. In fact, the latter replacing the first equation of Equation (3) are given by Equation (A1) [30]. Note that, for this set of equations as well as the following definitions in this section, the dependence on time, $\cdot(t)$. is omitted for better readability.

$$\begin{aligned} \dot{\phi} &= \omega_x + (\omega_y \sin\phi + w_z \cos\phi)\tan\theta \\ \dot{\theta} &= \omega_y \cos\phi - \omega_z \sin\phi \\ \dot{\psi} &= (\omega_y \sin\phi + \omega_z \cos\phi)\cos\theta^{-1} \end{aligned} \tag{A1}$$

In Equation (A1), $\boldsymbol{\omega}_B = \begin{bmatrix} \omega_x & \omega_y & \omega_z \end{bmatrix}^T$ and $\boldsymbol{\lambda} = \begin{bmatrix} \phi & \theta & \psi \end{bmatrix}^T$ is the set of Euler angles. Therefore, the complete system of equations in the vehicle's body-fixed reference frame is given by:

$$\begin{aligned} \dot{\boldsymbol{\lambda}} &= \begin{bmatrix} 1 & \sin\phi\tan\theta & \cos\phi\tan\theta \\ 0 & \cos\phi & -\sin\phi \\ 0 & \sin\phi\cos\theta^{-1} & \cos\phi\cos\theta^{-1} \end{bmatrix} \boldsymbol{\omega}_B \\ \dot{\boldsymbol{\omega}}_B &= J^{-1}\left[\mathbf{M}_{TVC,B} + \mathbf{M}_{aero,B} + \mathbf{M}_{fins,B} - \boldsymbol{\omega}_B \times J\boldsymbol{\omega}_B\right] \\ \dot{\mathbf{r}}_B &= \mathbf{v}_B \\ \dot{\mathbf{v}}_B &= \frac{1}{m}\left[\mathbf{F}_{TVC,B} + \mathbf{F}_{aero,B} + \mathbf{F}_{fins,B}\right] + \mathbf{R}_B^I \mathbf{g}_I - \boldsymbol{\omega}_B \times \mathbf{v}_B \end{aligned} \tag{A2}$$

where $\mathbf{r}_B = \begin{bmatrix} x_B & y_B & z_B \end{bmatrix}^T$, $\mathbf{v}_B = \begin{bmatrix} v_x & v_y & v_z \end{bmatrix}^T$, $\mathbf{R}_B^I$ represents the rotation matrix from the inertial reference frame to the vehicle's body-fixed reference frame, and $\mathbf{g}_I = \begin{bmatrix} g & 0 & 0 \end{bmatrix}^T$ is the gravitational field expressed in the inertial frame. The former is obtained by applying a 3-2-1 rotation sequence and given as follows:

$$\mathbf{R}_B^I = \begin{bmatrix} \cos\theta\cos\psi & \cos\theta\sin\psi & -\sin\theta \\ -\cos\phi\sin\psi + \sin\phi\sin\theta\cos\psi & \cos\phi\cos\psi + \sin\phi\sin\theta\sin\psi & \sin\phi\cos\theta \\ \sin\phi\sin\psi + \cos\phi\sin\theta\cos\psi & -\sin\phi\cos\psi + \cos\phi\sin\theta\sin\psi & \cos\phi\cos\theta \end{bmatrix} \tag{A3}$$

This formulation allows for a simpler management of the state and the control variables once the system is decomposed. In fact, considering Equation (A2), the state vector is $\mathbf{x} = \begin{bmatrix} \boldsymbol{\lambda}^T & \boldsymbol{\omega}_B^T & \mathbf{r}_B^T & \mathbf{v}_B^T \end{bmatrix} \in \mathbb{R}^{12}$, while $\mathbf{u} = \begin{bmatrix} \beta_{TVC,y} & \beta_{TVC,z} & \beta_{fin,y} & \beta_{fin,z} \end{bmatrix} \in \mathbb{R}^4$ is the control vector. Note that, for simplicity and for enabling the decoupling of the pitch and yaw planes [26], the thrust magnitude is directly taken from the guidance algorithm and is therefore not considered as a control variable.

The set Equation (A2) is linearized around the reference trajectory; therefore, the system can be rewritten in terms of perturbed variables with the symbol Δ. More particularly, we obtain the following state-space realization:

$$\Delta\dot{\mathbf{x}} = \mathbf{A} \cdot \Delta\mathbf{x} + \mathbf{B} \cdot \Delta\mathbf{u} \tag{A4}$$

where $\mathbf{A} \in \mathbb{R}^{12\times12}$ and $\mathbf{B} \in \mathbb{R}^{12\times4}$ are the Jacobian of the nonlinear equations with respect to the state and input variables. The details of the linearization assumptions and the decoupling considered is described hereafter.

Appendix A.1. Linearization of the 6-DoF Equations of Motion

To linearize the equations of motion, each term is replaced by its corresponding steady-state term plus a perturbation, e.g., $\xi = \xi_0 + \Delta\xi$ [46,47]. The steady-state terms are then removed by computing the steady-state solutions (i.e., by cancelling the vehicle acceleration).

Before displaying the perturbed equations obtained, it is necessary to define the assumptions considered. Let us recall that the TVC-generated force and moment, $\mathbf{F}_{TVC,B} \in \mathbb{R}^3$ and $\mathbf{M}_{TVC,B} \in \mathbb{R}^3$, are given by [26]:

$$\begin{aligned}\mathbf{F}_{TVC,B} &= T_{ref}\begin{bmatrix}\cos\beta_{TVC,y}\cos\beta_{TVC,z}\\ \cos\beta_{TVC,y}\sin\beta_{TVC,z}\\ -\sin\beta_{TVC,y}\end{bmatrix}\\ \mathbf{M}_{TVC,B} &= [\mathbf{x}_{PVP} - \mathbf{x}_{CG}] \times \mathbf{F}_{TVC,B}\end{aligned} \tag{A5}$$

The aerodynamic force and moment, $\mathbf{F}_{aero,B} \in \mathbb{R}^3$ and $\mathbf{M}_{aero,B} \in \mathbb{R}^3$, are:

$$\begin{aligned}\mathbf{F}_{aero,B} &= -QS_{ref}\begin{bmatrix}C_D\cos\alpha\cos\beta + C_L\sin\alpha\\ C_D\sin\beta\\ C_D\sin\alpha\cos\beta + C_L\cos\alpha\end{bmatrix} = -QS_{ref}\begin{bmatrix}C_{A,LV}(\alpha,\beta)\\ C_{Y,LV}(\beta)\\ C_{N,LV}(\alpha,\beta)\end{bmatrix}\\ \mathbf{M}_{aero,B} &= [\mathbf{x}_{CP} - \mathbf{x}_{CG}] \times \mathbf{F}_{aero,B}\end{aligned} \tag{A6}$$

It is assumed that $C_{A,LV}(\alpha,\beta)$ and $C_{N,LV}(\alpha,\beta)$ can be approximated as follows:

$$\begin{aligned}C_{A,LV}(\alpha,\beta) &\approx C_{A,LV}(\alpha) = C_D\cos\alpha + C_L\sin\alpha\\ C_{N,LV}(\alpha,\beta) &\approx C_{N,LV}(\alpha) = C_D\sin\alpha + C_L\cos\alpha\end{aligned} \tag{A7}$$

This rough approximation comes from the geometry of the launcher descent trajectory, which is usually mainly in the pitch plane. For this study, it enables an easier management of the aerodynamic coefficients. In fact, the latter are approximated thanks to an aerodynamic database computed from the effective angle of attack, α_{eff} [26]. For a more accurate consideration of the aerodynamics, the reader is referred to Ref. [24], where the coefficients are computed with computational fluid dynamics techniques and validated with wind-tunnel tests. Therefore, from Equations (A6) and (A7), we can approximate that [22]:

$$\begin{aligned}C_{A,LV}(\alpha_0+\Delta\alpha) &\approx C_{A,LV}(\alpha_0) + C_{A,LV\backslash\alpha}\Delta\alpha\\ C_{Y,LV}(\beta_0+\Delta\beta) &\approx C_{Y,LV}(\beta_0) + C_{Y,LV\backslash\beta}\Delta\beta\\ C_{N,LV}(\alpha_0+\Delta\alpha) &\approx C_{N,LV}(\alpha_0) + C_{N,LV\backslash\alpha}\Delta\alpha\end{aligned} \tag{A8}$$

where $C_{A,LV\backslash\alpha}$, $C_{Y,LV\backslash\beta}$, and $C_{N,LV\backslash\alpha}$ are the aerodynamic force gradients obtained through the aerodynamic coefficients look-up tables.

Concerning the steerable planar fins, the model described in Ref. [26] and taken from Ref. [29] implies that the total force and moment generated by the fins, $\mathbf{F}_{fins,B} \in \mathbb{R}^3$ and $\mathbf{M}_{fins,B} \in \mathbb{R}^3$, are given by:

$$\begin{aligned}\mathbf{F}_{fins,B} &= 2QS_{fin}\begin{bmatrix}C_{N,fin,z}(\gamma_{fin,z})\sin\beta_{fin,z} - C_{N,fin,y}(\gamma_{fin,y})\sin\beta_{fin,y}\\ C_{N,fin,z}(\gamma_{fin,z})\cos\beta_{fin,z}\\ C_{N,fin,y}(\gamma_{fin,y})\cos\beta_{fin,y}\end{bmatrix}\\ \mathbf{M}_{fins,B} &= 2QS_{fin}\begin{bmatrix}0\\ -(x_{fin}-x_{CG})C_{N,fin,y}(\gamma_{fin,y})\cos\beta_{fin,y}\\ (x_{fin}-x_{CG})C_{N,fin,z}(\gamma_{fin,z})\cos\beta_{fin,z}\end{bmatrix}\end{aligned} \tag{A9}$$

Recalling that $\gamma_{fin,y} = \beta_{fin,y} - \alpha$ and $\gamma_{fin,z} = -\beta_{fin,z} - \beta$, the normal fin forces can be linearized as follows:

$$\begin{aligned} C_{N,fin,y}(\gamma_{fin,y0} + \Delta\gamma_{fin,y}) &\approx C_{N,fin,y}(\gamma_{fin,y0}) + C_{N,fin,y\backslash\gamma}\Delta\gamma_{fin,y} \\ &\approx C_{N,fin,y}(\gamma_{fin,y0}) + C_{N,fin,y\backslash\gamma}\Delta\beta_{fin,y} - C_{N,fin,y\backslash\gamma}\Delta\alpha \\ C_{N,fin,z}(\gamma_{fin,z0} + \Delta\gamma_{fin,z}) &\approx C_{N,fin,z}(\gamma_{fin,z0}) + C_{N,fin,z\backslash\gamma}\Delta\gamma_{fin,z} \\ &\approx C_{N,fin,z}(\gamma_{fin,z0}) - C_{N,fin,z\backslash\gamma}\Delta\beta_{fin,z} - C_{N,fin,z\backslash\gamma}\Delta\beta \end{aligned} \tag{A10}$$

where $C_{N,fin,y\backslash\gamma}$ and $C_{N,fin,z\backslash\gamma}$ are the fin normal force gradients defined by:

$$\begin{aligned} C_{N,fin,y\backslash\gamma} &= 2\pi\left(\frac{AR_{fin}}{AR_{fin}+2}\right)\cos(\gamma_{fin,y0}) \\ C_{N,fin,z\backslash\gamma} &= 2\pi\left(\frac{AR_{fin}}{AR_{fin}+2}\right)\cos(\gamma_{fin,z0}) \end{aligned} \tag{A11}$$

with AR_{fin} being the aspect ratio of the fins.

Furthermore, the linearization of the equations of motion relies on a set of well-known small angle approximations, such as:

$$\begin{aligned} \cos\Delta\xi &= 1 \\ \sin\Delta\xi &= \Delta\xi \\ \tan\Delta\xi &= \Delta\xi \\ \cos(\xi_0 + \Delta\xi) &= \cos\xi_0 - \sin\xi_0\Delta\xi \\ \sin(\xi_0 + \Delta\xi) &= \sin\xi_0 + \cos\xi_0\Delta\xi \\ \tan(\xi_0 + \Delta\xi) &= \tan\xi_0 + (1 + \tan{\xi_0}^2)\Delta\xi \end{aligned} \tag{A12}$$

Finally, from this assumption and the definitions of the aerodynamic angles, it is possible to approximate the angle of attack, $\Delta\alpha$, and the sideslip angle, $\Delta\beta$, perturbations as functions of the lateral drift variations, respectively $\Delta\dot{z}_B$ and $\Delta\dot{y}_B$. More particularly, we have [44]:

$$\begin{aligned} \Delta\alpha &\approx \frac{\Delta v_z}{v_{x,0}} \\ \Delta\beta &\approx \frac{\Delta v_y}{||\mathbf{v}_B||_2} \end{aligned} \tag{A13}$$

Note that, in this paper, for simplicity, potential wind gusts are not considered and the local velocity variations (depending on the vehicle's rotation) due to the computation of the aerodynamic angles at the vehicle's CP or fin's positions instead of the vehicle's CG are neglected. For considering their corresponding perturbations, the reader is referred to Ref. [46].

Therefore, applying all these transformations to Equation (A2) componentwise yields:

$$
\begin{aligned}
\Delta\dot{\phi} &= (\omega_{y,0}\cos\phi_0\tan\theta_0 - \omega_{z,0}\sin\phi_0\tan\theta_0)\Delta\phi + \left[\omega_{y,0}\sin\phi_0(1+\tan{\theta_0}^2) + \omega_{z,0}\cos\phi_0(1+\tan{\theta_0}^2)\right]\Delta\theta \\
&\quad + \Delta\omega_x + \sin\phi_0\tan\theta_0\Delta\omega_y + \cos\phi_0\tan\theta_0\Delta\omega_z \\
\Delta\dot{\theta} &= -(\omega_{y,0}\sin\phi_0 + \omega_{z,0}\cos\phi_0)\Delta\phi + \cos\phi_0\Delta\omega_y - \sin\phi_0\Delta\omega_z \\
\Delta\dot{\psi} &= (\omega_{y,0}\cos\phi_0\cos{\theta_0}^{-1} - \omega_{z,0}\sin\phi_0\cos{\theta_0}^{-1})\Delta\phi + (\omega_{y,0}\sin\phi_0 + \omega_{z,0}\cos\phi_0)\tan\theta_0\cos{\theta_0}^{-1}\Delta\theta \\
&\quad + \sin\phi_0\cos{\theta_0}^{-1}\Delta\omega_y + \cos\phi_0\cos{\theta_0}^{-1}\Delta\omega_z \\
\Delta\dot{\omega}_x &= 0 \\
\Delta\dot{\omega}_y &= \frac{1}{J_N}\Bigg[-(J_A - J_N)\omega_{z,0}\Delta\omega_x - (J_A - J_N)\omega_{x,0}\Delta\omega_z \\
&\quad + \frac{(x_{CP} - x_{CG})QS_{ref}C_{N,LV\backslash\alpha} + 2(x_{fin} - x_{CG})QS_{fin}C_{N,fin,y\backslash\gamma}\cos\beta_{fin,y0}}{v_{x,0}}\Delta v_z \\
&\quad - (x_{CG} - x_{PVP})T_{ref}\cos\beta_{TVC,y0}\Delta\beta_{TVC,y} - 2(x_{fin} - x_{CG})QS_{fin}C_{N,fin,y\backslash\gamma}\cos\beta_{fin,y0}\Delta\beta_{fin,y}\Bigg] \\
\Delta\dot{\omega}_z &= \frac{1}{J_N}\Bigg[(J_A - J_N)\omega_{y,0}\Delta\omega_x + (J_A - J_N)\omega_{x,0}\Delta\omega_y \\
&\quad - \frac{(x_{CP} - x_{CG})QS_{ref}C_{Y,LV\backslash\beta} + 2(x_{fin} - x_{CG})QS_{fin}C_{N,fin,z\backslash\gamma}\cos\beta_{fin,z0}}{||\mathbf{v}_B||_2}\Delta v_y \\
&\quad + (x_{CG} - x_{PVP})T_{ref}\sin\beta_{TVC,y0}\sin\beta_{TVC,z0}\Delta\beta_{TVC,y} - (x_{CG} - x_{PVP})T_{ref}\cos\beta_{TVC,y0}\cos\beta_{TVC,z0}\Delta\beta_{TVC,z} \\
&\quad - 2(x_{fin} - x_{CG})QS_{fin}C_{N,fin,z\backslash\gamma}\cos\beta_{fin,z0}\Delta\beta_{fin,z}\Bigg] \\
\Delta\dot{x}_B &= \Delta v_x \\
\Delta\dot{y}_B &= \Delta v_y \\
\Delta\dot{z}_B &= \Delta v_z \\
\Delta\dot{v}_x &= g\sin\theta_0\cos\psi_0\Delta\theta + g\cos\theta_0\sin\psi_0\Delta\psi - v_{z,0}\Delta\omega_y + v_{y,0}\Delta\omega_z \\
&\quad + \left[\omega_{z,0} - \frac{2QS_{fin}C_{N,fin,z\backslash\gamma}\sin\beta_{fin,z0}}{m||\mathbf{v}_B||_2}\right]\Delta v_y - \left[\omega_{y,0} + \frac{QS_{ref}C_{A,LV\backslash\alpha} - 2QS_{fin}C_{N,fin,y\backslash\gamma}\sin\beta_{fin,y0}}{m\cdot v_{x,0}}\right]\Delta v_z \\
&\quad - \frac{1}{m}\Bigg[T_{ref}\sin\beta_{TVC,y0}\cos\beta_{TVC,z0}\Delta\beta_{TVC,y} + T_{ref}\cos\beta_{TVC,y0}\sin\beta_{TVC,z0}\Delta\beta_{TVC,z} \\
&\quad + 2QS_{fin}C_{N,fin,y\backslash\gamma}\sin\beta_{fin,y0}\Delta\beta_{fin,y} + 2QS_{fin}C_{N,fin,z\backslash\gamma}\sin\beta_{fin,z0}\Delta\beta_{fin,z}\Bigg] \\
\Delta\dot{v}_y &= -g(\sin\phi_0\sin\psi_0 + \cos\phi_0\cos\psi_0\sin\theta_0)\Delta\phi - g\cos\psi_0\cos\theta_0\sin\phi_0\Delta\theta + g(\cos\phi_0\cos\psi_0 + \sin\phi_0\sin\psi_0\sin\theta_0)\Delta\psi \\
&\quad + v_{z,0}\Delta\omega_x - v_{x,0}\Delta\omega_z - \omega_{z,0}\Delta v_x - \frac{1}{m}\Bigg[\frac{QS_{ref}C_{Y,LV\backslash\beta} + 2QS_{fin}C_{N,fin,z\backslash\gamma}\cos\beta_{fin,z0}}{||\mathbf{v}_B||_2}\Delta v_y \\
&\quad + T_{ref}\sin\beta_{TVC,y0}\sin\beta_{TVC,z0}\Delta\beta_{TVC,y} - T_{ref}\cos\beta_{TVC,y0}\cos\beta_{TVC,z0}\Delta\beta_{TVC,z} \\
&\quad + 2QS_{fin}C_{N,fin,z\backslash\gamma}\cos\beta_{fin,z0}\Delta\beta_{fin,z}\Bigg] \\
\Delta\dot{v}_z &= -g(\cos\phi_0\sin\psi_0 - \sin\phi_0\cos\psi_0\sin\theta_0)\Delta\phi - g\cos\psi_0\cos\theta_0\cos\phi_0\Delta\theta - g(\sin\phi_0\cos\psi_0 - \cos\phi_0\sin\psi_0\sin\theta_0)\Delta\psi \\
&\quad - v_{y,0}\Delta\omega_x + v_{x,0}\Delta\omega_y + \omega_{y,0}\Delta v_x - \frac{1}{m}\Bigg[\frac{QS_{ref}C_{N,LV\backslash\alpha} + 2QS_{fin}C_{N,fin,y\backslash\gamma}\cos\beta_{fin,y0}}{v_{x,0}}\Delta v_z \\
&\quad + T_{ref}\cos\beta_{TVC,y0}\Delta\beta_{TVC,y} - 2QS_{fin}C_{N,fin,y\backslash\gamma}\cos\beta_{fin,y0}\Delta\beta_{fin,y}\Bigg]
\end{aligned}
\tag{A14}
$$

From the set of Equation (A14), we can therefore derive the state-space realization of the system defined in Equation (A4). In fact, the latter describes the dynamics of the MIMO system, before decoupling the pitch and yaw planes.

Appendix A.2. Pitch Plane

As mentioned in the paper, due to the axial symmetry of the launch vehicle about the roll axis, the pitch and yaw axes can be assumed to be uncoupled. Therefore, the the design and analysis can be achieved in single planes. This assumption is only valid if the roll rate of the launcher is kept small ($\Delta\dot{\phi} \approx 0$), which is a standard assumption for launcher control design. Note that the vehicle is usually equipped with a roll and attitude control system, performing 3-axes control during the aerodynamic phase and roll rate control during the propelled phases [21]. Furthermore, the effects of the assumption of negligible roll rate assumption are usually examined ad hoc [48].

Therefore, considering that the roll angle ϕ is very close to 0 deg during the whole duration of the descent flight (and also that the reference roll angle is always 0, i.e., $\phi_0 = 0$), the attitude kinematics Equation (A1) becomes the following:

$$\begin{aligned} \dot{\phi} &= \omega_x \\ \dot{\theta} &= \omega_y \\ \dot{\psi} &= \omega_z \end{aligned} \tag{A15}$$

Note that we also assume that the pitch angle θ remains small. We further assume that the components of the vector $\boldsymbol{\omega}_B \times J\boldsymbol{\omega}_B$ are negligible since they are always smaller than 1 Nm. Finally, the last assumption concerns the terms $\omega_{y,0}\Delta v_x$ and $\omega_{z,0}\Delta v_x$, which are considered negligible for allowing the decoupling between longitudinal and lateral dynamics. More particularly, the following conditions hold:

$$\begin{aligned} \omega_{y,0}\Delta v_x &\ll \Delta v_z \\ \omega_{z,0}\Delta v_x &\ll \Delta v_y \end{aligned} \tag{A16}$$

With all these assumptions, with respect to the pitch dynamics, the state-space realization of Equation (A4) can be rewritten as follows:

$$\begin{bmatrix} \Delta\dot{\theta} & \Delta\ddot{\theta} & \Delta\dot{z}_B & \Delta\ddot{z}_B \end{bmatrix}^T = \mathbf{A}_\theta \begin{bmatrix} \Delta\theta & \Delta\dot{\theta} & \Delta z_B & \Delta\dot{z}_B \end{bmatrix}^T + \mathbf{B}_\theta \begin{bmatrix} \Delta\beta_{TVC,y} & \Delta\beta_{fin,y} \end{bmatrix}^T \tag{A17}$$

where the matrices $\mathbf{A}_\theta$ and $\mathbf{B}_\theta$ are defined by:

$$\mathbf{A}_\theta = \begin{bmatrix} 0 & 1 & 0 & 0 \\ 0 & 0 & 0 & \frac{\mu_{\alpha'}}{v_{x,0}} \\ 0 & 0 & 0 & 1 \\ -a_{0,\theta} & v_{x,0} & 0 & -\frac{N_{\alpha'}}{m \cdot v_{x,0}} \end{bmatrix}, \quad \mathbf{B}_\theta = \begin{bmatrix} 0 & 0 \\ -\mu_{TVC}\cos\beta_{TVC,y0} & -\mu_{fin,y,\gamma}\cos\beta_{fin,y0} \\ 0 & 0 \\ -\frac{T_{ref}}{m}\cos\beta_{TVC,y0} & \frac{N_{fin,y,\gamma}}{m}\cos\beta_{fin,y0} \end{bmatrix} \tag{A18}$$

with the following definitions:

$$\begin{aligned} N_{LV,\alpha} &= QS_{ref}C_{N,LV\backslash\alpha} \\ N_{fin,y,\gamma} &= 2QS_{fin}C_{N,fin,y\backslash\gamma} \\ N_{\alpha'} &= N_{LV,\alpha} + N_{fin,y,\gamma}\cos\left(\beta_{fin,y0}\right) \\ \mu_{LV,\alpha} &= \frac{N_{LV,\alpha}}{J_N}(x_{CP} - x_{CG}) \\ \mu_{fin,y,\gamma} &= \frac{N_{fin,y,\gamma}}{J_N}(x_{fin} - x_{CG}) \\ \mu_{TVC} &= \frac{T_{ref}}{J_N}(x_{CG} - x_{PVP}) \\ \mu_{\alpha'} &= \mu_{LV,\alpha} + \mu_{fin,y,\gamma}\cos\left(\beta_{fin,y0}\right) \\ a_{0,\theta} &= g\cos\left(\theta_0\right)\cos\left(\psi_0\right) \end{aligned} \tag{A19}$$

Appendix A.3. Yaw Plane

Similarly, the state-space realization of Equation (A4) with respect to the yaw dynamics is defined as follows:

$$\begin{bmatrix} \Delta\dot{\psi} & \Delta\ddot{\psi} & \Delta\dot{y}_B & \Delta\ddot{y}_B \end{bmatrix}^T = \mathbf{A}_\psi \begin{bmatrix} \Delta\psi & \Delta\dot{\psi} & \Delta y_B & \Delta\dot{y}_B \end{bmatrix}^T + \mathbf{B}_\psi \begin{bmatrix} \Delta\beta_{TVC,z} & \Delta\beta_{fin,z} \end{bmatrix}^T \quad \text{(A20)}$$

where the matrices $\mathbf{A}_\psi$ and $\mathbf{B}_\psi$ are defined by:

$$\mathbf{A}_\psi = \begin{bmatrix} 0 & 1 & 0 & 0 \\ 0 & 0 & 0 & -\frac{\mu_{\beta'}}{||\mathbf{v}_B||_2} \\ 0 & 0 & 0 & 1 \\ a_{0,\psi} & -v_{x,0} & 0 & -\frac{N_{\beta'}}{m||\mathbf{v}_B||_2} \end{bmatrix}, \quad \mathbf{B}_\psi = \begin{bmatrix} 0 & 0 \\ -\mu_{TVC}\cos\beta_{TVC,y0}\cos\beta_{TVC,z0} & -\mu_{fin,z,\gamma}\cos\beta_{fin,z0} \\ 0 & 0 \\ \frac{T_{ref}}{m}\cos\beta_{TVC,y0}\cos\beta_{TVC,z0} & -\frac{N_{fin,z,\gamma}}{m}\cos\beta_{fin,z0} \end{bmatrix} \quad \text{(A21)}$$

with:

$$\begin{aligned} N_{LV,\beta} &= QS_{ref}C_{Y,LV\backslash\beta} \\ N_{fin,z,\gamma} &= 2QS_{fin}C_{N,fin,z\backslash\gamma} \\ N_{\beta'} &= N_{LV,\beta} + N_{fin,z,\gamma}\cos(\beta_{fin,z0}) \\ \mu_{LV,\beta} &= \frac{N_{LV,\beta}}{J_N}(x_{CP} - x_{CG}) \\ \mu_{fin,z,\gamma} &= \frac{N_{fin,z,\gamma}}{J_N}(x_{fin} - x_{CG}) \\ \mu_{\beta'} &= \mu_{LV,\beta} + \mu_{fin,z,\gamma}\cos(\beta_{fin,z0}) \\ a_{0,\psi} &= g\cos(\psi_0) \end{aligned} \quad \text{(A22)}$$

References

1. Wall, M. Wow! SpaceX Lands Orbital Rocket Successfully in Historic First. 2015. Available online: https://www.space.com/31420-spacex-rocket-landing-success.html (accessed on 4 December 2023).
2. Jones, H.W. The Recent Large Reduction in Space Launch Cost. In Proceedings of the 48th International Conference on Environmental Systems, Albuquerque, NM, USA, 8–12 July 2018.
3. RocketLab. Neutron: The Mega Constellation Launcher. Available online: https://www.rocketlabusa.com/launch/neutron (accessed on 4 December 2023).
4. Blue Origin. New Glenn: Our Next (Really) Big Step—An Orbital Reusable Launch Vehicle That Will Build the Road to Space. 2019. Available online: https://www.blueorigin.com/new-glenn (accessed on 4 December 2023).
5. Deng, X. Long March-8 Rocket Likely to Try Out Vertical Landing in 2021: Chinese Developer. Available online: https://www.globaltimes.cn/page/202103/1217312.shtml (accessed on 4 December 2023).
6. Indian Space Research Organisation. Reusable Launch Vehicle-Technology Demonstration Program (RLV-TD). Available online: https://www.isro.gov.in/RLVTD.html (accessed on 4 December 2023).
7. Patureau de Mirand, A.; Bahu, J.M.; Gogdet, O. Ariane Next, a vision for the next generation of Ariane Launchers. *Acta Astronaut.* **2020**, *170*, 735–749. [CrossRef]
8. Sagliano, M.; Heidecker, A.; Hernández, J.M.; Farì, S.; Schlotterer, M.; Woicke, S.; Seelbinder, D.; Dumont, E. Onboard Guidance for Reusable Rockets: Aerodynamic Descent and Powered Landing. In Proceedings of the AIAA Scitech 2021 Forum, Virtual Event, 11–15 & 19–21 January 2021; American Institute of Aeronautics and Astronautics: Reston, VA, USA, 2021. [CrossRef]
9. Blackmore, L. Autonomous Precision Landing of Space Rockets. *Bridge Front. Eng.* **2016**, *4*, 15–20.
10. Szmuk, M.; Reynolds, T.P.; Açıkmeşe, B. Successive Convexification for Real-Time Six-Degree-of-Freedom Powered Descent Guidance with State-Triggered Constraints. *J. Guid. Control Dyn.* **2020**, *43*, 1399–1413. [CrossRef]
11. Sagliano, M. Generalized hp Pseudospectral-Convex Programming for Powered Descent and Landing. *J. Guid. Control Dyn.* **2019**, *42*, 1562–1570. [CrossRef]
12. Liu, X. Fuel-Optimal Rocket Landing with Aerodynamic Controls. *J. Guid. Control Dyn.* **2019**, *42*, 65–77. [CrossRef]
13. Simplício, P.; Marcos, A.; Bennani, S. Guidance of Reusable Launchers: Improving Descent and Landing Performance. *J. Guid. Control Dyn.* **2019**, *42*, 2206–2219. [CrossRef]
14. Roux, C.; Cruciani, I. Scheduling Schemes and Control Law Robustness in Atmospheric Flight of VEGA. In Proceedings of the 7th International ESA Conference on Guidance, Navigation and Control Systems, Tralee, County Kerry, Ireland, 2–5 June 2008.
15. Mooij, E. *Linear Quadratic Regulator Design for an Unpowered, Winged Re-Entry Vehicle*; Number 03 in 08 Astrodynamics and Satellite Systems; Delft University Press: Delft, The Netherlands, 1998.

16. Doyle, J.; Glover, K.; Khargonekar, P.; Francis, B. State-space solutions to standard H2 and H∞ control problems. *IEEE Trans. Autom. Control* **1989**, *34*, 831–847. [CrossRef]
17. Apkarian, P.; Noll, D. Nonsmooth H∞ Synthesis. *IEEE Trans. Autom. Control* **2006**, *51*, 71–86. [CrossRef]
18. Du, W. Dynamic Modeling and Ascent Flight Control of Ares-I Crew Launch Vehicle. Ph.D. Thesis, Iowa State University, Ames, IA, USA, 2010.
19. Saussie, D.; Barbes, Q.; Berard, C. Self-scheduled and structured H-Infinity synthesis: A launch vehicle application. In Proceedings of the 2013 American Control Conference, Washington, DC, USA, 17–19 June 2013; IEEE: Piscataway, NJ, USA, 2013. [CrossRef]
20. Ganet-Schoeller, M.; Desmariaux, J.; Combier, C. Structured Control for Future European Launchers. *Aerosp. Lab* **2017**, *13*, 1–10. [CrossRef]
21. Navarro-Tapia, D.; Marcos, A.; Simplicio, P.; Bennani, S.; Roux, C. Legacy recovery and robust augmentation structured design for the VEGA launcher. *Int. J. Robust Nonlinear Control* **2019**, *29*, 3363–3388. [CrossRef]
22. Simplicio, P.; Marcos, A.; Bennani, S. New Control Functionalities for Launcher Load Relief in Ascent and Descent Flight. In Proceedings of the 8th European Conference for Aeronautics and Space Sciences, Madrid, Spain, 1–4 July 2019. [CrossRef]
23. Sagliano, M.; Tsukamoto, T.; Heidecker, A.; Maces Hernandez, J.A.; Farì, S.; Schlotterer, M.; Woicke, S.; Seelbinder, D.; Ishimoto, S.; Dumont, E. Robust Control for Reusable Rockets via Structured H-infinity Synthesis. In Proceedings of the 11th International ESA Conference on Guidance, Navigation & Control Systems, Virtual Event, 22–25 June 2021.
24. Sagliano, M.; Hernández, J.A.M.; Fari, S.; Heidecker, A.; Schlotterer, M.; Woicke, S.; Seelbinder, D.; Krummen, S.; Dumont, E. Unified-Loop Structured H-Infinity Control for Aerodynamic Steering of Reusable Rockets. *J. Guid. Control Dyn.* **2023**, *46*, 815–837. [CrossRef]
25. Iannelli, A.; Gkouletsos, D.; Smith, R.S. Robust Control Design for Flexible Guidance of the Aerodynamic Descent of Reusable Launchers. In Proceedings of the AIAA SCITECH 2023 Forum, National Harbor, MD, USA, 23–27 January 2023; American Institute of Aeronautics and Astronautics: Reston, VA, USA, 2023. [CrossRef]
26. De Oliveira, A.; Lavagna, M. Development of a Controlled Dynamics Simulator for Reusable Launcher Descent and Precise Landing. *Aerospace* **2023**, *10*, 993. [CrossRef]
27. Robbiani, T.; Sagliano, M.; Topputo, F.; Seywald, H. Fast Desensitized Optimal Control for Rocket Powered Descent and Landing. In Proceedings of the AIAA SCITECH 2024 Forum, Orlando, FL, USA, 8–12 January 2024; American Institute of Aeronautics and Astronautics: Reston, VA, USA, 2024. [CrossRef]
28. Gaudet, B.; Furfaro, R. Integrated and Adaptive Guidance and Control for Endoatmospheric Missiles via Reinforcement Meta-Learning. In Proceedings of the AIAA SCITECH 2023 Forum, National Harbor, MD, USA, 23–27 January 2023; American Institute of Aeronautics and Astronautics: Reston, VA, USA, 2023. [CrossRef]
29. Simplício, P.; Marcos, A.; Bennani, S. Reusable Launchers: Development of a Coupled Flight Mechanics, Guidance, and Control Benchmark. *J. Spacecr. Rocket.* **2020**, *57*, 74–89. [CrossRef]
30. Mooij, E. *The Motion of a Vehicle in a Planetary Atmosphere*; Faculty of Aerospace Engineering, Delft University of Technology: Delft, The Netherlands, 1994.
31. Committee on Extension to the Standard Atmosphere. *U.S. Standard Atmosphere 1976*; Technical Memorandum NASA-TM-X-74335; NASA: Washington, DC, USA, 1976.
32. De Oliveira, A.; Lavagna, M. Assessment of Reusable Launch Vehicles Re-entry Dynamics Control Effectiveness with Enhanced Aerodynamics Modelling. In Proceedings of the 73rd International Astronautical Congress (IAC), Paris, France, 18–22 September 2022.
33. Açıkmeşe, B.; Ploen, S.R. Convex Programming Approach to Powered Descent Guidance for Mars Landing. *J. Guid. Control Dyn.* **2007**, *30*, 1353–1366. [CrossRef]
34. Szmuk, M.; Açıkmeşe, B.; Berning, A.W. Successive Convexification for Fuel-Optimal Powered Landing with Aerodynamic Drag and Non-Convex Constraints. In Proceedings of the AIAA Guidance, Navigation, and Control Conference, San Diego, CA, USA, 4–8 January 2016; American Institute of Aeronautics and Astronautics: Reston, VA, USA, 2016. [CrossRef]
35. Grant, M.; Boyd, S. CVX: MATLAB Software for Disciplined Convex Programming, Version 2.1. 2014. Available online: http://cvxr.com/cvx (accessed on 4 December 2023).
36. Domahidi, A.; Chu, E.; Boyd, S. ECOS: An SOCP solver for embedded systems. In Proceedings of the 2013 European Control Conference (ECC), Zurich, Switzerland, 17–19 July 2013; IEEE: Piscataway, NJ, USA, 2013. [CrossRef]
37. Sagliano, M.; Seelbinder, D.; Theil, S.; Lu, P. Six-Degree-of-Freedom Rocket Landing Optimization via Augmented Convex–Concave Decomposition. *J. Guid. Control Dyn.* **2024**, *47*, 20–35. [CrossRef]
38. De Oliveira, A.; Lavagna, M. Robust Control Design via Structured H-infinity for the Atmospheric Re-entry of Reusable Launchers. In Proceedings of the 12th International ESA Conference on Guidance, Navigation and Control Systems, Sopot, Poland, 12–16 June 2023.
39. Simplício, P.; Bennani, S.; Marcos, A.; Roux, C.; Lefort, X. Structured Singular-Value Analysis of the VEGA Launcher in Atmospheric Flight. *J. Guid. Control Dyn.* **2016**, *39*, 1342–1355. [CrossRef]
40. De Oliveira, A. Guidance and Control System Design for Reusable Launch Vehicle Descent and Precise Landing. Ph.D. Thesis, Department of Aerospace Science & Technology, Politecnico di Milano, Milan, Italy, 2023.
41. Navarro-Tapia, D. Robust and Adaptive TVC Control Design Approaches for the VEGA Launcher. Ph.D. Thesis, Department of Aerospace Engineering, University of Bristol, Bristol, UK, 2019.

42. Doyle, J.C. Analysis of Feedback Systems with Structured Uncertainties. *IEE Proc. D-Control Theory Appl.* **1982**, *129*, 242–250. [CrossRef]
43. Skogestad, S. *Multivariable Feedback Control: Analysis and Design*; John Wiley & Sons, Inc.: New York, NY, USA, 1996.
44. Greensite, A.L. *Analysis and Design of Space Vehicle Flight Control Systems. Volume VII—Attitude Control During Launch*; Technical Report NASA-CR-826, NASA Contractor Report; NASA: Washington, DC, USA, 1967.
45. Boelitz, F. Kistler launch assist platform return burn control. In Proceedings of the Guidance, Navigation, and Control Conference and Exhibit, Portland, OR, USA, 9–11 August 1999; American Institute of Aeronautics and Astronautics: Reston, VA, USA, 1999. [CrossRef]
46. Simplício, P. Guidance and Control Elements for Improved Access to Space: From Planetary Landers to Reusable Launchers. Ph.D. Thesis, Department of Aerospace Engineering, University of Bristol, Bristol, UK, 2019.
47. Zipfel, P. *Modeling and Simulation of Aerospace Vehicle Dynamics*, 2nd ed.; AIAA Education Series; AIAA: Reston, VA, USA, 2007.
48. Roux, C.; Cruciani, I. Roll Coupling Effects on the Stability Margins for VEGA Launcher. In Proceedings of the AIAA Atmospheric Flight Mechanics Conference and Exhibit, Hilton Head, SC, USA, 20–23 August 2007; American Institute of Aeronautics and Astronautics: Reston, VA, USA, 2007. [CrossRef]